Tumor initiating cells escape tumor immunity via CCL8 from tumor-associated macrophages in mice

Shuang Chen[1*], Chensong Huang[1*], Kang Li[1*], Maosheng Cheng[1*], Caihua Zhang[1*], Jianqi Xiong[1], Guoli Tian[3], Ruoxing Zhou[1], Rongsong Ling[1], Xiaochen Wang[1], Gan Xiong[2], Zhihui Zhang[1], Jieyi Ma[1], Yan Zhu[1], Bin Zhou[4#], Liang Peng[5#], Zhenwei Peng[1#], Heping Li[2#], Demeng Chen[1#]

1. Department of Medical Oncology; Department of Pancreato-Biliary Surgery; Department of Radiation Oncology, Cancer Center; Center for Translational Medicine, The First Affiliated Hospital of Sun Yat-sen University, Guangzhou 510080, China.
2. Department of Medical Oncology, Sun Yat-sen Memorial Hospital, Sun Yat-sen University, Guangzhou, 510080, China.
3. Hospital of Stomatology, Sun Yat-sen University, Guangzhou, 510080, China.
4. State Key Laboratory of Cell Biology, Shanghai Institute of Biochemistry and Cell Biology, Center for Excellence in Molecular Cell Science, Chinese Academy of Sciences; University of Chinese Academy of Sciences, Shanghai, 200031, China.
5. Senior Department of Oncology, the Fifth Medical Center of PLA General Hospital, Beijing, 100071, China.

*. These authors contributed equally.

#. Address correspondence to: Demeng Chen, Center for Translational Medicine, The First Affiliated Hospital of Sun Yat-sen University, 58 Zhongshan Road II, Guangzhou, Guangdong 510080, China. Email: chendm29@mail.sysu.edu.cn. Phone: +86 20-87618634. Heping Li, Department of Oncology, Sun Yat-sen Memorial Hospital, Sun Yat-sen University, 107 Yanjiang West Road, Guangzhou, Guangdong 510080, China. Email: liheping@mail.sysu.edu.cn. Phone: +86 13710873975. Zhenwei Peng, Department of Radiation Oncology, Cancer Center, The First Affiliated Hospital of Sun Yat-sen University, 58 Zhongshan Road II, Guangzhou, Guangdong 510080, China. Email: pzhenw@mail.sysu.edu.cn. Phone:

+86 20-87755766. Liang Peng, Senior Department of Oncology, the Fifth Medical Center of PLA General Hospital, NO.8 East Street, Fengtai District, Beijing, 100071, China. Email: pengliang@301hospital.com.cn, Phone: +86 13901317123. Bin Zhou, State Key Laboratory of Cell Biology, Shanghai Institute of Biochemistry and Cell Biology, Center for Excellence in Molecular Cell Science, Chinese Academy of Sciences; University of Chinese Academy of Sciences, No. 320 Yueyang Road, Shanghai 200031, China. Email: zhoubin@sibs.ac.cn.

The authors have declared that no conflict of interest exists.

Abstract

Tumor-initiating cells (TICs) play a key role in cancer progression and immune escape. However, how TICs evade immune elimination remains poorly characterized. Combining single-cell RNA sequencing (scRNA-seq), dual-recombinase-based lineage tracing, and other approaches, we identified a WNT-activated subpopulation of malignant cells that act as TICs in vivo. We found intensive reciprocal interactions between TICs and immune regulatory tumor-associated macrophages (Reg-TAMs) via GAS6-AXL/MERTK signaling pathways, which facilitated the immune escape of TICs. Our study employed chemical inhibitors and *Axl*/*Mertk* conditional double knockout mice to demonstrate that inhibiting the interaction between TIC-derived GAS6 and AXL/MERTK in Reg-TAMs reactivated anti-tumor immune responses. We identified CCL8 as a critical mediator of the GAS6/AXL/MERTK pathway, primarily by inhibiting regulatory T cell (Treg) infiltration into the tumor. Furthermore, the AXL/MERTK signaling blockade sensitized tumor cells to anti-PD-1 treatment. Thus, we elucidated a detailed mechanism by which TICs evade tumor immunity, providing insights into strategies to eradicate TICs that escape conventional immunotherapy.

Keywords: Tumor-initiating cells (TICs), GAS6-AXL/MERTK, Immune Escape.

Main

As the second most common primary liver cancer, intrahepatic cholangiocarcinoma (ICC) is highly aggressive with a poor prognosis. The majority of ICC patients (>70%) are already at advanced stages at the time of diagnosis and cannot be surgically treated due to locally advanced or metastatic disease(1, 2). Thus far, effective therapeutic strategies for patients with ICC are limited. In addition, the highly heterogeneous nature of ICC at both genetic and phenotypic levels often leads to treatment failure and drug resistance.

Evidence suggests that tumor-initiating cells (TICs), a rare self-renewing population with multilineage differentiation potential and immune evasive properties, drive tumor heterogeneity(3). Historically, TICs in ICC have been characterized by markers such as KIT, SALL4, CD44, and SOX2(4). However, traditional approaches to identifying TICs often disrupt their architecture and interactions with the tumor microenvironment (TME). In addition, evidence shows that immune evasion is a key feature distinguishing TICs from non-TICs(5), but how TICs in ICC evade immune surveillance and how they shape an immunosuppressive TME remains unclear. Therefore, elucidating this mechanism and the immunological characteristics of TICs in ICC will improve our understanding of ICC development. To do so, it is crucial to pinpoint the TIC population within their niche in vivo. Lineage tracing has become a well-suited approach for delineating the tumor cell of origin and tumor heterogeneity in mouse models(6). Moreover, the fast-advancing technique of single-cell RNA sequencing (scRNA-seq) has allowed us to gain deeper insights into tumor heterogeneity and interplay within the tumor ecosystem(7).

In this study, we performed scRNA-seq to explore the tumor heterogeneity of murine ICC. We identified 18 cell types based on signature genes, categorized into six major groups: epithelium, stromal, NKT, B cells, MoMϕDc, and neutrophils in mouse ICC. These findings are highly consistent with online patient ICC scRNA-seq data(8). Further analysis revealed that a Wnt-activated subcluster of malignant epithelial cells could potentially give rise to other subclusters. We used a dual-recombinase-based lineage tracing system to verify these findings and track Wnt-activated epithelial cells

(AXIN2^{+}KRT19^{+}) in the mouse ICC model. We found that these cells are responsible for ICC development and progression. We then constructed a cell-cell interaction network based on scRNA-seq data. We found that Wnt-activated malignant epithelial cells interact intensively with immune regulatory tumor-associated macrophages (Reg-TAMs) via the GAS6-AXL/MERTK pathway. Functionally, inhibition of the GAS6-AXL/MERTK pathway led to repression of CCL8 expression in Reg-TAMs and impaired stemness of TICs in mouse ICC. Finally, we observed a synergistic effect of AXL/MERTK inhibitor with anti-PD-1 treatment on ICC. These results provide a rationale for the combination of AXL/MERTK inhibitor and anti-PD-1 antibody in ICC, and these findings might ultimately help identify a more effective combination regimen to elicit stronger antitumor responses.

Results

Single-cell sequencing and cell type identification in murine ICC

To investigate the tumor ecosystem and molecular signature in ICC, we performed hydrodynamic tail vein injection of HA-tagged AKT and YapS127A plasmid (AKT/Yap) with Sleeping Beauty (SB) plasmids in 6–8-week-old C57BL/6 mice (WT) (9, 10) (Fig. 1A). We detected multiple lesions of various sizes in mouse livers 6 weeks post-injection (Fig. 1A and B). Three independent pathologists from the first affiliated hospital of Sun Yat-sen University (FAH-SYSU) reviewed H&E, KRT19 immunohistochemistry (IHC), and immunofluorescence (IF) slides. These lesions were validated as cholangiocellular by positive KRT19 and negative HNF4A staining (Fig. 1B and C). Additionally, the AKT/Yap-induced ICC exhibited high proliferation, marked by MKI67 (Fig. 1C).

Subsequently, we dissected the ICC lesions macroscopically for generation of scRNA-seq profiles from two mice using 10× Genomics sequencing (Fig. 1D). After quality control and unsupervised clustering based on differentially expressed genes, we identified 18 cell types, categorized into six major groups: epithelium (*Krt19, Krt7, Krt8*), stromal (*Cdh5, Pecam1, Col1a2*), neutrophils (*S100a9, S100a8, Retnlg*), MoMϕDc (*Csfr1, C1qa, Vcan, H2-Ab1*), NKT (*Cd3d, Gzmb, Klrd1*), and B cells (*Cd79a, Igkc, Iglc2*) (Fig. 1E and G; Fig. S1A). A similar distribution was observed in both mouse ICC samples (Fig. 1F).

Next, we compared murine scRNA-seq data with a human ICC dataset of 14 samples(8). Six major cell clusters matched between datasets, showing high consistency and confirming dataset quality (Fig. S1B-F).

WNT-activated cells act as TICs in mouse ICC

To study the mechanisms regulating ICC development, we reclustered murine epithelial cells into 4 subclusters, C0-C3 (Fig. 2A). We then used three trajectory inference analyses to measure transcriptional dynamics and characterize the differentiation process of these epithelial subclusters. First, RNA velocity analysis showed that the epithelial C2 subcluster gave rise to both C0 and C3 subclusters and

further to C1 via C0 (Fig. 2B). Secondly, CytoTRACE analysis revealed that C2 cells were more undifferentiated/less differentiated (Fig. 2C). Lastly, pseudo-temporal analysis (Monocle2) indicated that C2 cells exhibit higher progenitor properties and give rise to other epithelial clusters (Fig. 2D). This suggests that C2 is a progenitor population that may give rise to other cell types. Further pathway analysis with GSVA based on KEGG pathways demonstrated diverse molecular subtypes, with C2 enriched in WNT signaling, key pathways for stemness maintenance (Fig. 2E)(11). Moreover, C2 showed higher WNT pathway scores compared to other subclusters, as assessed using the WNT signaling pathway gene set from the C2 modules of MSigDB (Fig. S2A). Interestingly, subcluster C3, not C2, was enriched in DNA replication, mismatch repair, and cell cycle pathways, with higher cell cycle scores (Fig. 2E, S2B), indicating that C2 cells are not actively proliferating.

To investigate whether our finding of TICs in mouse models could faithfully recapitulate human ICC, we performed CytoTRACE analysis on malignant epithelial cells from each patient sample (Fig. S2C). Our results showed that epithelial cells with higher CytoTRACE scores tended to express higher levels of *CTNNB1* (Fig. S2C). Furthermore, correlation analysis using cholangiocarcinoma datasets of The Cancer Genome Atlas (TCGA-CHOL) showed WNT pathway genes (*AXIN2*, *CTNNB1*, *LEF1*) positively correlated with TICs signature genes (*KIT*, *SALL4*, *CD44*, *SOX2*) (Fig. S2D-G).

To test whether WNT-activated epithelial cells could act as TICs in ICC, we generated a dual-recombinase-based lineage tracing system (*Krt19-DreER; Axin2-CreER; R26-Ai66*) mouse model. This model labels $KRT19^+AXIN2^+$ cells with tdTomato (Tom) upon tamoxifen administration, enabling the tracking of $KRT19^+AXIN2^+$ (Tom^+) cell dynamics during ICC tumorigenesis (Fig. 2F). Additionally, we conducted a time course experiment to track Tom^+ cells following hydrodynamic injection and observed the appearance of Tom^+ cells 2 weeks after injection (Fig. S3A-C). We then continued to monitor the dynamics of Tom^+ cells during ICC progression. Two weeks after hydrodynamic injection, tamoxifen was administered to the mice (Fig. 2G). From day 3 to week 3, after tamoxifen injection,

we observed rapid expansion and progression of Tom^+ cells in tumor nodules (Fig. S3D-F). Similarly, ICC induced using AKT and NICD (AKT/NICD)(10) also identified $KRT19^+AXIN2^+$ cells as a key source for ICC progression (Fig. S3G-I). Through scRNA-seq data, we found high expression of *Sox4* and *Klf6* in the C2 epithelial cell cluster, with *Sox4* and *Klf6* being associated with the maintenance of cancer stem cell stemness(12, 13). Furthermore, IF staining confirmed that most Tom^+ cells are positive for SOX4 and KLF6 (Fig. 2H-N). GSVA analysis identified key markers for the other three subclusters: *Atp6v1f, Scp2,* and *Mki67*. IF staining showed a gradual increase in $Tom^+ATP6V1F^+$, Tom^+SCP2^+, and Tom^+EdU^+ cells from day 3 to week 3 post-tamoxifen labeling (Fig. 2O-R). Furthermore, limiting dilution assays demonstrated higher tumorigenic potential in Tom^+ cells compared to Tom^- ICC cells (Fig. 2S-U).

To examine whether targeting $KRT19^+AXIN2^+$ cells in ICC impairs ICC progression, we generated *Krt19-DreER; Axin2-CreER; R26-Ai66-DTR* (DTR hereafter) mice (Fig. 3A)(14). In this model, two weeks after hydrodynamic injection, tamoxifen and diphtheria toxin (DT) treatment enabled ablation of $KRT19^+AXIN2^+$ cells (Fig. 3B). Results showed depletion of $KRT19^+AXIN2^+$ cells and a decrease in the other three cell subclusters, as confirmed by IF staining of RFP, EdU, SCP2, and ATP6V1F (Fig. 3C-F). This dramatically inhibited liver indices, measured as liver-to-body weight ratios (Fig. 3G and H). Moreover, ablation of $KRT19^+AXIN2^+$ cells resulted in fewer and smaller ICC tumors than controls (Fig. 3I-K). Consistently, IHC of KRT19 revealed markedly reduced KRT19-positive signals in the treatment group (Fig. 3L-N). The number of MKI67-positive cells markedly decreased, while apoptosis (active-caspase3) increased in ICC after $KRT19^+AXIN2^+$ cell ablation compared to controls (Fig. S3K-N).

Next, we investigated the role of canonical Wnt/β-catenin signaling in maintaining TICs in murine ICC by treating *Krt19-DreER, Axin2-CreER, R26-Ai66* and WT mice with XAV-939, a potent tankyrase inhibitor targeting Wnt/β-catenin signaling (Fig. 3O). Western blot analysis showed that XAV-939 suppressed the elevation of phosphorylated LRP6, total β-catenin, and nuclear β-catenin, as well as the decreased phosphorylated β-catenin levels in ICC TICs, with no change in LRP6 expression (Fig. S3J), indicating

effective inhibition of Wnt/β-catenin signaling. XAV-939 treatment suppressed ICC development (Fig. 3P-W; Fig. S3O-R). Lineage tracing revealed reduced Tom^+ cells (Fig. 3X and Y), suggesting that Wnt/β-catenin signaling is essential for $KRT19^+AXIN2^+$ TICs in ICC. Additionally, IF staining revealed decreased C0, C1, and C3 subclusters upon Wnt/β-catenin inhibition (Fig. 3Z).

Cell-cell interactions between ICC epithelial cells and other cell types

Emerging evidence shows that the TME regulates TICs' plasticity and immune escape(15). To investigate cell interactions in ICC, we constructed a cell-cell communication network using CellChat and identified distinct interactions (Fig. 4A). Notably, mouse ICC epithelial cells exhibited stronger ligand-receptor interactions with MoMϕDC populations (Fig. 4A). To investigate these interactions in detail, mouse MoMϕDC cells were partitioned into subclusters: Monocytes, Reg-TAMs, Angio-TAMs, DC1, DC2, and DC3 (Fig. S4A), similar lineages were found in human MoMϕDC (Fig. S4C). Gene expression for major myeloid subsets is shown in Fig. S5B and S5D. Unsupervised mouse and human myeloid subclusters clustering using orthologous genes revealed a one-to-one relationship (Fig. S4E and F).

Then, we conducted CellphoneDB analysis to map ligand-receptor pairs and found that GAS6-AXL/MERTK interactions, which promote the immunosuppressive TME(16), were highly enriched between ICC epithelium and Reg-TAMs (Fig. 4B). Furthermore, we found that *Gas6* expression was markedly elevated in the WNT^{hi} epithelial subcluster compared to the WNT^{low} epithelial subclusters (Fig. 4C). Both in mouse and human samples, *Axl*/*Mertk* (*AXL*/*MERTK*) were predominantly expressed in Reg-TAMs (Fig. 4D and Fig. S4G). Flow cytometry analysis of ICC samples 3 days post-lineage tracing showed that GAS6 levels were higher in Tom^+ ICC cells than in Tom^- ICC cells (Fig. 4E, F), and AXL and MERTK were enriched in Reg-TAMs (Fig. 4G, H). Additionally, human ICC scRNA-seq data showed higher CytoTRACE scores and upregulated *GAS6* (Fig. S2C). Both human ICC scRNA-seq and TCGA-CHOL data revealed higher *GAS6* in tumor cells, with positive correlations to WNT signaling genes (Fig. S4H-J).

GAS6-AXL/MERTK interactions between epithelial cells and Reg-TAMs play important roles in mouse ICC development

To explore the role of GAS6-AXL/MERTK interactions in ICC, we treated *Krt19-DreER; Axin2-CreER; R26-Ai66* ICC and WT ICC mice with a GAS6 neutralizing antibody (Fig. 4I). GAS6 antibody-treated mice exhibited delayed tumor burden and improved survival (median 66 days) compared to controls (median 45 days) (Fig. 4J-K). After 6 weeks, GAS6 antibody treatment markedly reduced Tom^+ cells (Fig. 4L and M) and decreased $KRT19^+$ and $MKI67^+$ cells (Fig. S5A-H). Histological analysis also revealed an increase in active-$Caspase3^+$ cells, suggesting the key role of GAS6 in cholangiocarcinogenesis (Fig. S5I and J).

To explore the prognostic value of GAS6 in ICC, IHC staining was performed on patient ICC tissue microarrays from two cohorts (clinical characteristics in Supplementary Tables S1 and S2). Tumors were categorized into high and low GAS6 groups using the median GAS6-positive signal as the cutoff. Representative images of GAS6 IHC staining for high- and low-density positive signals are presented in Fig 4N and 4Q. In the Sun Yat-Sen University Cancer Center (SYSUCC) cohort (n = 159), the GAS6-high group had markedly poorer overall survival (OS) and disease-free survival (DFS) than the GAS6-low group (Fig. 4N-P). Similar results were observed using the FAHSYSU cohort (n = 200) (Fig. 4Q-S). High GAS6 levels were also substantially associated with tumor stage and grade (Fig. S5K and L). We generated *Axin2-creER; Gas6$^{flox/flox}$* mice and conducted AKT/Yap/SB hydrodynamic injection (Fig. S6A). *Gas6* knockout was validated by western blot (Fig. S6I). Conditional deletion of *Gas6* in $Axin2^+$ cells improved ICC phenotype severity (Fig. S6B-H). Flow cytometry revealed reduced $CD4^+$ T cell and Tregs infiltration, with increased $CD8^+$ T cells in ICC tumor from *Axin2-creER; Gas6$^{flox/flox}$* mice, while NK and NKT cell frequencies remained unchanged (Fig. S6J-Q). To investigate TIC-derived GAS6 suppressing tumor immunity via AXL/MERTK on Reg-TAMs, we used *Krt19-DreER; Axin2-creER; R26-Ai66* mice for AKT/Yap/SB hydrodynamic injection and sorted Reg-TAMs and $Epcam^+Tom^+$ TICs. Co-culture results showed elevated AXL, MERTK, and AKT phosphorylation in Reg-TAMs with TICs (Fig. S6R and S), confirming that GAS6 on

TICs promotes AXL, MERTK, and AKT phosphorylation in Reg-TAMs(17).

To explore the role of AXL/MERTK in Reg-TAMs and ICC development, we treated ICC-bearing mice with R428, an inhibitor of tyrosine kinases, including AXL and MERTK (17). R428-treated mice showed substantially reduced tumor burden and improved survival (Fig. 5A-C; Fig. S7A-F). Cell proliferation was moderately inhibited after 6 weeks of treatment (Fig. S7G, H), while apoptosis markedly increased (Fig. S7I, J). To assess the effect of R428 inhibition on the interaction between Reg-TAMs and TICs, $Epcam^{+}Tom^{+}$ TICs and Reg-TAMs from ICC-bearing Krt19-DreER; Axin2-creER; R26-Ai66 mice were sorted and co-cultured with or without R428. Western blot showed downregulation of p-AXL, AKT, p-AKT, p-MERTK, and NF-kB1 in Reg-TAMs (Fig. S7K). Lineage tracing assays revealed reduced expansion of TICs in R428-treated mice (Fig. 5D). In addition, *Lyz2-creER;* $Axl^{flox/flox}$*;* $Mertk^{flox/flox}$ mice (*Axl* and *Mertk* conditional double knockout, cDKO) were generated and used for AKT/Yap/SB hydrodynamic injection (Fig. S7P). The efficiency of the double knockout was confirmed by western blot (Fig. S8A). As expected, *Axl* and *Mertk* knockout in myeloid cells alleviated ICC phenotype severity (Fig. S7Q-W).

Since AXL/MERTK are mainly expressed in mouse Reg-TAMs, we conducted flow cytometry to examine tumor-infiltrated macrophages. Flow cytometry revealed that the number of $CD11b^{+}$ $F4/80^{+}$ macrophages in R428-treated ICC samples was comparable to controls (Fig. S7L-M; Fig. S14A). Surprisingly, the percentages of $F4/80^{+}MRC1^{+}$ / $F4/80^{+}CD86^{+}$ double-positive cells were similar (Fig. S7N-O), indicating that AXL/MERTK inhibition does not affect macrophage polarization. This was further confirmed in ICC samples treated with a GAS6 antibody (Fig. S5M-P). Moreover, *Axl* and *Mertk* double knockout in ICC did not alter macrophage numbers or polarization (Fig. S8C-F). Our data suggest that AXL/MERTK signaling may not be essential for the number and polarization of macrophages.

Given that the R428 treatment inhibited mouse ICC tumor growth, we examined the major tumor-infiltrating T lymphocytes. Tumors from R428-treated mice showed a reduction in $CD4^{+}$ T cells and an increase in $CD8^{+}$ T cells (Fig. 5E-G; Fig. S14B). However, no marked differences were observed in $CD45^{+}CD3^{+}$ $NK1.1^{+}$ NKT cells and

$CD45^+CD3^-$ $NK1.1^+$ NK cells (Fig. 5H-J). Similarly, *Axl* and *Mertk* double knockout reduced the proportion of $CD4^+$ T cells in ICC samples without marked changes in NK/NKT cell numbers (Fig. S8G-L). To dissect the functional link between AXL/MERTK in Reg-TAMs and T cells in ICC, we isolated Reg-TAMs from R428-treated ICC for RNA-seq. We identified 483 up-regulated and 1,001 down-regulated genes in R428-treated Reg-TAMs (Fig. 5K, Table S3). KEGG analysis revealed that down-regulated genes were primarily involved in the NF-kB, TNF, MAPK, Chemokine, and PI3K-Akt pathways (Fig. 5L). Western blot confirmed reduced levels of p-AXL, p-AKT, AKT, p-MERTK, and NF-kB1 in Reg-TAMs after R428 treatment (Fig. 5M) and qRT-PCR verified the repression of target genes (Fig. 5N).

To identify the potential functional mediator of AXL/MERTK in Reg-TAMs, we examined the top 10 down-regulated genes in both mouse and human scRNA-seq datasets. We found that *Ccl8* was the only secreted factor specifically expressed in Reg-TAMs (Table S3, Fig. 5O and Fig. S9A). R428 treatment substantially reduced CCL8 levels in Reg-TAMs, as confirmed by ELISA (Fig. 5P). Similarly, both ELISA and western blot showed reduced CCL8 levels after *Axl* and *Mertk* double knockout (Fig. S8A, C). *CCL8* expression strongly correlated with *CD163*, *AXL*, and *MERTK* in TCGA-CHOL dataset (Fig. S9B). It has been shown that CCL8 affects Tregs infiltration(18), and we observed a marked decrease in Tregs in the R428-treated group (Fig.5Q and R; Fig. S9C). Similarly, *Axl* and *Mertk* double knockout also reduced Treg numbers (Fig. S8N and Q).

CCL8 is one of the key mechanisms of the GAS6/AXL/MERTK signaling pathway in ICC formation

Then, to assess the effects of CCL8 on mouse ICC, we generated *Lyz2-creER; Ccl8* $^{flox/flox}$ mice for AKT/Yap hydrodynamic injection (Fig. 6A). As expected, *Ccl8* deletion in myeloid cells prolonged survival and reduced the severity of ICC (Fig. 6B and C; Fig. S10A-F). The frequency of NK and NKT cells remained unchanged, while $CD4^+$ T cells and Tregs decreased, and $CD8^+$ T cells increased (Fig. 6D-G). Additionally, flow cytometry showed a slight reduction in the infiltration of cDCs,

pDCs, monocytes, macrophages, and PMN cells in ICC tumor samples from *Lyz2-creER*; *Ccl8*$^{flox/flox}$ mice (Fig. S10G-P). Moreover, we used *Ccl8*-/- mouse for AKT/Yap hydrodynamic injection (Fig. S9C). The efficiency of *Ccl8* knockout was confirmed by western blot (Fig. S9D). Notably, *Ccl8* deletion led to prolonged survival and reduced ICC severity (Fig. S9E-F, Fig. S9G-P). Consistently, flow cytometry analysis showed a decrease in $CD4^+$ T cells and Tregs, an increase in $CD8^+$ T cells, and unchanged NK and NKT cells in ICC samples from *Ccl8*-/- mice (Fig. S9Q-X).

We then wondered whether CCL8 overexpression could reverse the effects of R428 on mouse ICC. Mice treated with R428 and systemic CCL8 overexpression exhibited notably reversed delayed ICC formation and prolonged survival induced by R428 treatment (Fig. 6H- J). Lineage tracing assays revealed that CCL8 reversed the inhibition of $KRT19^+AXIN2^+$ TICs expansion in R428-treated mice (Fig. 6K). Flow cytometry showed that CCL8 substantially affected the infiltration of Tregs, $CD4^+$ T, and $CD8^+$ T cells but not NK and NKT cells (Fig. 6L-M). Consistently, histological and IHC staining confirmed that CCL8 rescued the inhibition of tumor formation and apoptosis induction by R428, with cell proliferation largely unchanged (Fig. S12K-N). Similarly, in *Lyz2-creER*; *Axl*$^{flox/flox}$; *Mertk*$^{flox/flox}$ mice, *Axl* and *Mertk* double knockout led to a slight reduction in the infiltration of cDCs, pDCs, monocytes, and PMN cells, but these changes showed no marked differences. Furthermore, CCL8 administration after the double knockout did not notably affect the infiltration of these cells (Fig. S11). These results suggest that AXL/MERTK signaling promotes ICC formation partially via CCL8. To evaluate whether *Axl* and *Mertk* in macrophages influence the function of $CD8^+$ T and Tregs, further co-culture of Reg-TAMs with $CD8^+$ T and naïve $CD4^+$ T cells showed no notable differences in $CD8^+$ T cell proliferation or Treg differentiation, regardless of *Axl/Mertk* double knockout or CCL8 addition (Fig. S12A-B).

Inhibition of GAS6-AXL/MERTK signaling sensitizes murine ICC cells to anti-PD-1 treatment

The markedly decreased Treg infiltration in murine ICC after R428 treatment encouraged us to investigate whether combining R428 with anti-PD-1 therapy could

further inhibit tumor growth. ICC-bearing mice were treated with vehicle, R428, anti-PD-1, or R428+anti-PD-1 (Fig. 7A). All treatments suppressed tumor growth compared to the vehicle, but anti-PD-1 monotherapy only modestly improved survival and reduced tumor burden. In contrast, R428 monotherapy and combination therapy had more pronounced effects (Fig. 7B-J). Analysis of tumor tissues revealed that $MKI67^+$ cell percentages were reduced only in the combination group, while active-$caspase3^+$ cell percentages were highest in the combination group (Fig. 7K-N). Tumor-associated macrophages (TAM) frequency and Reg-TAM percentages were unchanged (Fig.7O-Q). Flow cytometry showed that R428 or R428+anti-PD-1 reduced Treg infiltration and increased $CD8^+$ T cell infiltration, while anti-PD-1 alone did not notably affect Tregs and only slightly increased $CD8^+$ T cells (Fig. S13).

Discussion

TICs contribute to intratumoral heterogeneity and high mortality in ICC. We reported immune-evasive Wnt-responsive TICs in ICC and their crosstalk with Reg-TAMs via the GAS6-AXL/MERTK pathway. This interaction enables TICs to evade destruction by adaptive immunity through Treg recruitment via CCL8 cytokine secretion. Our study reveals a mechanism by which TICs in ICC establish immune evasion.

In this study, we performed scRNA-seq to investigate the molecular mechanism of TICs in ICC using an AKT/Yap hydrodynamic injection mouse model, which recapitulates the morphological and molecular features of human ICC(9, 10). A comparison of our mouse and human ICC scRNA-seq datasets revealed substantial overlap in cellular composition and molecular signatures. Trajectory inference consistently showed Wnt-activated malignant cells at the top of the ICC progression hierarchy, suggesting them as potential TICs. Few studies have used lineage tracing to explore ICC TICs. Combining a dual-recombinase lineage tracing system and cellular ablation assay, we provided substantial evidence to support that Wnt-activated cells are the bone fide TICs in ICC.

Previous reports show that while non-TICs can form tumors in highly immunocompromised mice but fail to do so in partially immunocompromised mice, TICs can give rise to tumors in both scenarios, suggesting immune evasion is one of the key features that distinguish TICs from non-TICs(5). The interaction between TICs stemness and immunogenicity in ICC remains largely unexplored. TICs escape immunosurveillance through mechanisms such as upregulating immune checkpoints, repressing T-cell activation, and downregulating MHC-1 expression (19, 20). TAMs play a critical role in TIC immune evasion through reciprocal interactions. TICs recruit and activate macrophage precursors via chemokines and periostin (21, 22), while TAMs support TICs maintenance by secreting cytokines like IL-6, IL-1b, TNFA, TGFB, CCL2, and CCL5 (23). Macrophages are traditionally divided into M1 and M2 types. M1 macrophages ($CD86^{+}/CD80^{+)}$ are critical to suppress tumor growth, while M2 macrophages ($CD206^{+}/CD163^{+)}$ display protumor properties (24). However, our

analysis and online scRNA-seq datasets found distinguishing M1-M2 polarization in ICC TAMs challenging. Instead, we identified regulatory TAMs (Reg-TAMs) expressing *Mrc1*, *C1qa*, *C1qb*, and *C1qc*. Remaining Angio-TAMs express *Arg1*, *Bnip3*, and *Mif*, showing an intermediate phenotype between monocytes and Reg-TAMs.

In our study, we showed that treatment of GAS6 neutralizing antibody led to inhibited expansion of Wnt-activated TICs in mouse ICC. Previously, GAS6 has been shown as a potent factor for β-catenin stabilization and subsequent TCF/Lef transcriptional activation(25). GAS6 seemed to determine the Wnt activity in TICs in ICC. However, the upstream event of GAS6 remains unknown. It will be helpful to determine whether altering the genomic landscape relevant to GAS6 might be a driving event of ICC initiation in a larger patient cohort. In addition, the extent to which GAS6 inhibition can directly inhibit the function of TICs requires further investigation, given that blocking GAS6 also caused significant changes in the TME that are heavily involved in TICs regulation. Notably, GAS6 expression is highly correlated with WNT-related genes in TCGA-CHOL datasets. Additionally, GAS6 may be a prognostic marker for ICC based on results from two independent cohorts.

The PD-1/PD-L1 pathway and Tregs are critical for TICs to evade immune surveillance and suppress antitumor immunity(26, 27). We found that the treatment of R428 synergizes with anti-PD-1 therapy to mouse ICC, resulting in less numerous infiltrated Tregs, partially due to inhibition of CCL8. The exact details of how R428 modulates Tregs infiltration have not been fully explored. A previous study has shown that CCL8 recruits $CCR5^+$ Tregs (18). In addition, ablation of tumor-infiltrating Treg cells expressing CCR8, one of the primary receptors for CCL8, can elicit antitumor immunity and improve the efficacy of anti-PD-1 therapy(28). In the future, functional assays will be helpful to validate the role of these receptors in Tregs.

In conclusion, our study highlights the critical role of GAS6-AXL/MERTK interactions between TICs and TAMs in mediating TICs immune evasion in ICC. These findings provide insights into how TICs manipulate TAMs to hijack the immune system. Blocking AXL/MERTK with R428 substantially reduced Tregs recruitment to tumors. Consequently, R428 combined with anti-PD-1 therapy dramatically suppressed ICC

growth in mice, suggesting this strategy holds promising clinical potential.

Methods and materials

Sex as a biological variable

Both male and female animals were examined in this study, and similar findings were reported for both sexes.

Constructs and reagents

The constructs used for mouse hydrodynamic injection in this study, including AKT (pT3-EF1a-HA-myr-AKT, mouse, Addgene 31789), Yap (pT3-EF1a-YapS127A, human, Addgene 86497), NCID (pT3-EF1a-NICD1, mouse, Addgene 46047) and SB (pCMV-Sleeping Beauty transposase) were courtesy of Dr. Xin Chen (University of California, San Francisco, USA). Plasmids were isolated and purified using the Endofree Maxi Plasmid Kit (DP117-TA, Tiangen Biotech Co., Ltd).

Mice, hydrodynamic injection, lineage tracing and drug treatment

Axin2-CreER (018867) mice were purchased from The Jackson Laboratory. C57BL/6, *Krt19-DreER* (T056046), *Ccl8*$^{flox/flox}$ (T013044), *Gas6*$^{flox/flox}$ (T010051), *Axl*$^{flox/flox}$ (T009234), *Mertk*$^{flox/flox}$(T007888) and *Lyz2-CreER* (T052789) mice were purchased from GemPharmatech. *R26-Ai66-DTR* (NM-KI-190086) mouse strain was purchased from Shanghai Model Organisms. *Ccl8*-/- mice were kindly given by Dr. Hongli Zhou (Second Affiliated Hospital of Army Medical University, Chongqing, China). BALB/c-nu/nu mice were purchased from the Laboratory Animal Center at Sun Yat-Sen University. *R26-Ai66-tdTomato* mice were generated as previously described(29). All animals in this study were maintained under specific pathogen-free conditions, housed under a 12-hour light/dark cycle, and given ad libitum access to food and water. For ICC induction, we hydrodynamically injected 30μg of Yap or 20μg of NICD, along with 4 μg of AKT and 1 μg of transposase plasmids in 6 to 10-week-old WT or transgenic mice as previously described(10, 30).

For lineage tracing, tamoxifen (T5648, Sigma) was dissolved in ethanol and diluted with corn oil to a 10% ethanol: tamoxifen: corn oil mixture at 20 mg/mL. Dre

or Cre was activated by intraperitoneal injection of tamoxifen (100 μg/g body weight) for five consecutive days. For ablation of DTR-expressing cells, mice were injected intraperitoneally with 500 ng boluses of un-nicked diphtheria toxin (DT) (150, List Biologics), every other day. For treatment, XAV-939 (T1878-100, TargetMol) was given intraperitoneally at 2.4 mg/mL, 250 μL once daily(31). R428 (S2841, Selleck) was administered by oral gavage at 25 mg/kg twice daily(17). GAS6 neutralizing antibody (AB885, R&D) was injected intraperitoneally at 2 mg/kg twice a week(32). Recombinant MCP-2/CCL8 (HY-P7239, MedChemExpress) was injected at 1 μg in 200 μL PBS once daily(33). Anti-PD1 (BE0146, BioXcell) was administered intraperitoneally at 200 μg/mouse every three days(34). Controls received vehicle or IgG isotype control antibody. All treatments began the second week after hydrodynamic injection and continued until the day before sample collection.

Tissue preparation, cell isolation and scRNA-seq

WT mice were euthanized by CO2 inhalation 6 weeks after hydrodynamic injection with AKT/Yap/SB for liver collection. Malignant lesions were dissected using a microscope, minced into one mm^3 pieces, and digested with a Tumor Dissociation Kit (130-096-730, Macs Miltenyi Biotec) at 37°C for 45 min using gentleMACS Dissociator (130-093-235, Macs Miltenyi Biotec). The reaction was stopped with PBS, filtered through a 40 μm Falcon strainer (352340, Corning), and centrifuged at 300 × g for 5 min. The pellet was treated with ACK Lysing Buffer (A1049201, Thermo Fisher) on ice for 5 min, and dead cells were removed using MS columns from the Dead Cell Removal Kit (130-090-101, Macs Miltenyi Biotec). Live cells were resuspended in PBS with 0.04% BSA and counted using Countess 3 Automated Cell Counter (Thermo Fisher). Single cells were loaded into 10× Genomics Chromium Controller (aiming for 20,000 cells per sample), and scRNA-seq libraries were prepared with Chromium Single Cell 3' Reagent Version 2 Kit (10× Genomics) and sequenced on MGISEQ2000 System (BGI).

Processing and clustering of scRNA-seq data

Following sequencing, raw reads were demultiplexed using the mkfastq command from Cell Ranger (Version 4.0.0, 10× Genomics) and aligned to the mm10 reference genome (GRCm38.91) using the count command to generate cell-gene-barcode matrices. These matrices were then merged using Seurat (version 4.0.0) for downstream analysis. Low-quality cells and genes were filtered by excluding genes detected in <3 cells, cells with <200 or >5,000 genes, >10% mitochondrial/hemoglobin gene expression, and doublets identified by DoubletFinder. After quality control, data were integrated and normalized using Seurat's "harmony" function, retaining 18,410 cells for further analysis.

After data integration and normalization, we performed principal component analysis (PCA) on highly variable genes using the RunPCA function in Seurat. Cell clustering was done with the FindClusters, and the clusters were visualized using UMAP with the RunUMAP function. Each cluster was annotated using canonical marker genes identified by the FindAllMarkers function with a likelihood-ratio test. To assess the cell cycle status, we applied the CellCycleScoring function based on markers for the S and G2/M phases.

We also downloaded available scRNA-seq datasets from the Genome Sequence Archive in the National Genomics Data Center (HRA000863), including 14 pairs of human iCCA tumor and non-tumor liver tissues. All quality control, normalization, and downstream analysis were performed using Seurat unless otherwise specified.

Gene correlation analysis within the TCGA-CHOL cohort was performed using Encyclopedia of RNA Interactomes (ENCORI), a state-of-the-art, openly licensed platform for RNA interactome data.

Bulk RNA-seq analysis

Data were filtered using SOAPnuke (v1.5.2) by removing reads with sequencing adapter, low-quality base (>20%), or unknown base ('N'> 5%). Clean reads were then obtained and stored in FASTQ format. Clean reads were mapped to the reference genome with HISAT2 (v2.0.4) and aligned to the reference coding gene set with Bowtie2 (v2.2.5). Gene expression was quantified using RSEM (v1.2.12), and

differential expression analysis was conducted using DESeq2 (v1.4.5) with Q value ≤ 0.05. KEGG enrichment analysis was performed on annotated differentially expressed genes based on a Hypergeometric test. The significance levels of terms and pathways were corrected for by Bonferroni with a rigorous threshold (Q value ≤ 0.05).

Major cell-type clustering and marker gene identification

We categorized the scRNA-seq cells into six major subpopulations: epithelial, stromal, B cells, neutrophils, MoMϕDC, and NKT. After refining stromal, MoMϕDC, and NKT clusters, specific gene markers were identified using FindAllMarkers, and clusters were annotated based on canonical marker gene expression. After reintegrating these six major subpopulations, we performed principal component analysis (PCA) on the list of highly variable genes using the RunPCA function in Seurat and visualized the clustering using UMAP, ultimately identifying 18 distinct subclusters.

Reconstructing cellular trajectories of tumor cells

Different trajectory inference approaches were used to infer differentiation trajectories of tumor cells. RNA velocity analysis was performed using the velocyto R package (Version 0.6) on unspliced and spliced matrices generated from the 10× scRNA-seq bam files. RNA velocity and plots were generated using the standard velocyto workflow. The CytoTRACE R package (Version 0.3.3) estimated the differentiation state of cells, with a score from 0 to 1 indicating stemness (higher score) or differentiation (lower score). Pseudo-temporal analysis was performed using the Monocle 2 R package (Version 2.24.0), selecting genes expressed in >10 cells with q-values < 0.0005 for analysis, followed by dimensionality reduction and trajectory construction using default methods.

Gene set variation analysis (GSVA)

Pathway analysis was performed using KEGG gene sets from the MSigDB database (version 7.2) with GSVA analysis (GSVA package, version 1.44.2) under standard settings to assign pathway activity estimates to individual cells. Differential

pathway activities between epithelial sub-clusters were obtained using the Limma package (version 3.52.2).

Analysis of interaction between cell types

To reveal the cell-cell interactions in the mouse ICC scRNAseq dataset, we used the Cellchat R package (Version 1.4.0) to infer potential communication networks. Ligand-receptor pairs between epithelial cells and MoMϕDC cells were mapped using the CellPhoneDB tool (version 2.1.7) with the default pipeline.

Gene sets enrichment analysis

We calculated WNT scores for epithelial cells using AddModuleScore function in Seurat, with the "WNT_SIGNALING" gene set from the C2 modules of MSigDB.

Mouse-human ICC cell typses comparison Sankey diagram and heatmaps

We used the publicly available human ICC single-cell HRA000863 dataset to compare mouse cell types and human ICC. Orthogonal genes were identified in both species, and mutual nearest neighbors were used to integrate cells, correcting batch effects. The RunFastMNN function (SeuratWrappers, v0.1.0) generated an integrated matrix after Seurat's sctransform identified variable genes. Seurat was then used for cell-type identification and grouping. A Sankey diagram was created to visualize cell type origins(35). Mouse and human ICC cell types were analyzed at single-cell and transcriptome levels, and dendrograms and heatmaps were made for comparison across species(36).

Histology, immunohistochemistry and multi-color immunohistochemistry detection

Mouse liver tissues were fixed in neutral formalin, embedded in paraffin, and sectioned at 5 μm. Sections were de-paraffinized, rinsed in PBS, and subjected to antigen retrieval using sodium citrate antigen retrieval solution (C02-02002, Bioss). Endogenous peroxidase was blocked with 3% H_2O_2 (CS7730, G-clone) for 10 min,

followed by blocking with 5% BSA for 30 min at 37 °C. Sections were incubated overnight at 4 °C with primary antibodies: HNF4A (ab41898, Abcam), MKI67 (NB500-170, Novus), Cytokeratin 19 (ab52625, Abcam), RFP (600-401-379, Rockland), Cleaved Caspase-3 (9661S, CST), GAS6 (DF8659, Affinity), F4/80 (ab100790, Abcam), MRC1 (ab64693, Abcam), ATP6V1F (HPA062011, sigma-aldrich) and SCP2 (MA5-44821, Thermo Fisher Scientific), AXL (AF7793, Affinity), MERTK (ab300136, Abcam). Sections were then incubated with HRP-labeled secondary antibodies at 37 °C for 30 min. Sections were stained with DAB, examined under a microscope, washed with PBS, and counterstained with hematoxylin, followed by dehydration, clearing, and mounting. Images were acquired using a digital section scanner (KF-PRO-20 MAGSCANCNER KFBIO, KFBIO).

For immunofluorescence, sections were pre-incubated with 5% BSA for 30 min, then incubated with primary antibodies overnight at 4°C. HRP-labeled secondary antibodies were applied at room temperature for 15 min. Dyes 520, 570, and 650 (PANOVUE) were used to visualize antigen-binding sites. Images were captured using a confocal microscope (ZEISS LSM880 with Airyscan).

To assess cell proliferation in vivo, EdU (100 mg/mice) was injected intraperitoneally and chased for 90 min. EdU incorporation was marked using a Click-iT EdU Alexa Fluor 488 Kit (C10337, Thermo Fisher Scientific) per the manufacturer's protocol.

Flow cytometry analysis and fluorescence-activated cell sorting

Single-cell suspensions of mouse ICC samples were prepared as described. Cells were washed in staining buffer (2% bovine growth serum in PBS) and resuspended to 1 × 10^7 cells/mL. For extracellular staining, cells were stained with antibodies in the staining buffer for 1 hour at 4°C. For intracellular staining, cells were fixed for 45 min using the Foxp3/Transcription factor staining buffer kit (Tonbo Biosciences, TNB-0607-KIT), washed, and stained overnight at 4°C with antibodies in 1× permeabilization buffer. The following antibodies and dyes were used for flow cytometry: CD45 PE-Cyanine7 (Tonbo Biosciences, 60-0451), CD3 APC (Tonbo

Biosciences, 20-0032), CD8a VioletFluo 450 (Tonbo Biosciences, 75-1886), CD4 FITC (eBioscience, 35-0042), FOXP3 PerCP/Cy5.5 (Tonbo Biosciences, 55-5773-U100), CD25 PE (Tonbo Biosciences, 50-0251-U100), CD206 APC (Biolegend, 141708), F4/80 PE (Biolegend, 137014), F4/80 PerCP/Cy5.5 (eBioscience, 2349828), CD86 PerCP/Cy5.5 (Biolegend, 105028), NK1.1 PerCP/Cy5.5 (Tonbo, 65-5941), CD11b Violet Fluorescence 500 (Tonbo Biosciences, 85-0112), Ghost Dye™ Red 780 (Tonbo Biosciences,13-0865), EpCAM APC (Invitrogene, B358247), AXL BV421 (BD Biosciences, 748028), Ghost dye™ red 710 (Tonbo Biosciences, 13-0871-T100), MERTK APC-CY7 (Invitrogene, 47-5751-80), GAS6 FITC (Bioss, bs-7549R-BF488), Siglech APC (Biolegend, 129611), MHCII FITC (Tonbo Biosciences, 35-5321-U100), CD11C VioletFluo 450 (Tonbo Biosciences, 75-0114-U025), LY6G APC-CY7 (Biolegend, 127623), LY6C (Invitrogene, 45-5932-80). Samples were analyzed using a flow cytometer (CytoFLEX, Beckman Coulter), and data were analyzed using NovoExpress software (version 2.0).

For sorting of intratumoral Reg-TAMs, single-cell suspensions of digested tumors were stained with Ghost Dye™ Red 780 for 30 min, followed by 500 ng Fc blocker (anti-CD16/32, Elabscience) for 15 min and then with anti-CD45 PE-Cyanine7, CD11b Violet 500, F4/80 PE, and CD206 APC (Biolegend) in 1 ml staining buffer (PBS + 2% FBS) for 30 min at 4°C. Live $CD206^+$ macrophages were sorted on a flow cytometer (FACSAria Fusion, BD).

Limiting dilution assay

Limit-dilution transplantation in nude mice: FACS-sorted cells ($EpCAM^{+/}Tomato^+$ or $EpCAM^{+/}Tomato^-$) from primary ICC of *Krt19-DreER*; *Axin2-CreER*; *R26-Ai66* mice were used. Five-week-old BALB/c-nu/nu nude mice were anesthetized with 87.5 mg/kg Ketamine/12.5 mg/kg Xylazine and subcutaneously injected in the dorsal region. Mice were then placed in a sterile laminar flow chamber and monitored for 24 hours for vital signs.

Human Tissue collection

ICC tissues and adjacent tissues were collected from patients who underwent surgery at the First Affiliated Hospital of Sun Yat-sen University or Sun Yat-sen University Cancer Center. Informed written consent was obtained from all patients prior to the experiment.

Western blotting

To detect the protein expression of Reg-TAMs, Reg-TAMs were isolated and sorted from tumors as previously described, then lysed in ice-cold RIPA buffer (P0013B, Beyotime) with protease and phosphatase inhibitors (4693132001, Roche) using a gentleMACS Dissociator (130-093-235, Miltenyi Biotec). For mouse liver tissue, tissues were dissected and lysed in the same buffer. Protein concentration was measured using the BCA assay (23227, Thermo Fisher). Equal protein amounts were separated by 10% SDS-PAGE (EpiZyme, PG11X), transferred to PVDF membranes (Merck Millipore, IPVH00010), and probed with antibodies against AXL (ab215205, Abcam), p-AXL (AF8523, Affinity), MERTK (ab300136, Abcam), p-MERTK (PA5-143631, ThermoFisher Scientific), GAS6 (DF8659, Affinity), β-Catenin (ab32572, Abcam), phospho-β-Catenin (9561, CST), LRP6 (3395, CST), phospho-LRP6 (2568, CST), CCL8 (55062, SAB), GAPDH (2118S, CST), NF-kB1 (13586, CST), AKT (9272, CST), and phospho-AKT (9271, CST). After washing, blots were incubated with HRP-conjugated secondary antibody (SA00001-2, Proteintech), and bands were visualized using ECL (Tanon, 180-5001).

Treg differentiation assay

Naïve $CD4^+$ T cells were isolated from C57BL/6 mice using the EasySep™ Mouse Naïve $CD4^+$ T Cell Isolation Kit (19765, Stemcell Technologies). Reg-TAMs were sorted by flow cytometry and co-cultured with naïve $CD4^+$ T cells in lymphocyte culture medium (88-581-cm, Corning) at 37°C in 5% CO_2 for 3 days. IL-2 (10 ng/ml, PKSM041320, Elabscience) and TGF-β1 (10 ng/ml, PRP110618, Abbkine) were added to promote Tregs differentiation. After 72 hours, cells were analyzed by flow cytometry for FOXP3 and CD25 expression to assess Treg differentiation.

Proliferation assay for $CD8^+$ T cells

To assess the impact of Reg-TAMs on $CD8^+$ T cell proliferation, $CD8^+$ T cells were isolated from ICC-bearing C57BL/6 mice using flow cytometry, and Reg-TAMs were sorted from ICC tumors with or without *Axl* and *Mertk* knockout. The $CD8^+$ T cells were resuspended in PBS (1x10^7 cells/ml) and labeled with 5 μM CFSE (565082, Biosciences) for 10 minutes at RT, then quenched with lymphocyte medium containing10% FBS. After washing, Reg-TAMs were added to the co-culture in a medium with 10% FBS, and IL-2 (10 ng/ml, PKSM041320, Elabscience). Cells were incubated at 37°C, 5% CO_2 for 72 hours, and then analyzed by flow cytometry for $CD8^+$ T cell proliferation.

Enzyme-Linked Immunosorbent Assay (ELISA)

CCL8 concentrations in Reg-TAMs of ICC were measured using ELISA kits (JONLN, JL10984) according to the manufacturer's instructions. Briefly, 100 μL samples were incubated on 96-well plates at 37°C for 1 h, followed by biotinylated primary antibody incubation for 1 h. After washing, streptavidin-HRP was added and incubated for 30 min, then washed, and TMB substrate was added for 15 min in the dark. Absorbance was measured using a TECAN Infinite M200Pro reader.

RNA extraction and qRT-PCR analysis

The total RNA of sorted macrophages was extracted with AG RNAex Pro Reagent (Accurate Biotechnology, AG21102) according to the manufacturer's instructions. The RNA concentration was measured using a NanoDrop spectrophotometer (Nano-300). qRT-PCR was performed using PerfectStart Green qPCR SuperMix (TransGen Biotech, AQ601) on a Bio-Rad CXF96 real-time system (Bio-Rad). Relative quantity was calculated using an internal control.

Statistical analyses

In this study, numerical data and histograms were presented as the mean ± SD.

Statistical parameters are provided in figure legends. All experiments were performed at least twice. The data shown are representative or a combination of independent experiments. A two-tailed Student's t-test was used for comparisons between two groups, with $p < 0.05$ considered significant. For multiple group comparisons ($n>2$), one-way ANOVA was used. Survival analysis was performed with the log-rank test. Limiting dilutions were analyzed using Extreme Limiting Dilution Analysis software (http://bioinf.wehi.edu.au/software/elda/). $p < 0.05$ was considered significant. All statistical analyses were conducted using GraphPad Prism 9 software.

Study approval

All animal experiments were approved by the Institutional Animal Care and Use Committee (IACUC), Sun Yat-Sen University (protocol number SYSU-IACUC-2021-000138, Guangzhou, China). All patients provided written informed consent prior to undergoing surgical treatment.

Data availability

The raw sequencing data reported in this paper (including scRNA-seq and Bulk RNA-seq data) have been deposited in the Genome Sequence Archive in the National Genomics Data Center under the accession numbers CRA008695 and CRA008863. The analysis of public datasets was retrieved from HRA000863(8). The remaining data can be found in the article, supplementary information, or in the Supporting Data Values file.

Code availability statement

This study does not use any custom computer code or algorithm.

Resource availability

LEAD CONTACT AND MATERIALS AVAILABILITY

Further information and requests for resources and reagents should be directed to

and will be fulfilled by the Lead Contact, Demeng Chen (chendm29@mail.sysu.edu.cn).

Ackonwledgments

We thank the members of the Lin, Chen, Yuan, Zhang and Zhou labs for the reagents, mouse strains, helpful discussions and data-analysis support. We thank the Sun Yat-sen University Cancer Center for providing clinical samples. This work is supported by National Natural Science Foundation of China (82173362, 81872409, 82304069 and 81974443), China Postdoctoral Science Foundation (2023M734003), Natural Science Foundation of Guangdong Province (2018A030313610), the Open Funding of the State Key Laboratory of Oral Diseases (SKLOD2021OF02), Guangdong Basic and Applied Basic Research Foundation (2019A1515110110, 2018A030313176), Guangzhou Science and Technology Plan Project (202201010927) and the Guangdong Basic and Applied Basic Research Foundation (2024A1515030145).

Author contributions

Conceptualization, S.C., M.C., K.L., X.W., and D.C.; Methodology, S.C., G.T., R.Z., M.C., R.L., C.Z., Z.C., G.X., and D.C.; Data Analysis and Curation, S.C., K.L., M.C., Y.Z., Y.L., Z.Z., and D.C.; Investigation and Validation, S.C., K.L., M.C., Y.Z., Y.L., Z.Z., and D.C.; Resources, C.H., B.Z., Z.P., L.P., D.C., and H.L.; Writing, S.C., K.L., and D.C. Supervision and funding acquisition, L.P., and D.C.

Declaration of interests

The authors declare no potential conflicts of interest.

References

1. Rizvi S, Khan SA, Hallemeier CL, Kelley RK, and Gores GJ. Cholangiocarcinoma - evolving concepts and therapeutic strategies. *Nat Rev Clin Oncol.* 2018;15(2):95-111.
2. Banales JM, Marin JJG, Lamarca A, Rodrigues PM, Khan SA, Roberts LR, et al. Cholangiocarcinoma 2020: the next horizon in mechanisms and management. *Nat Rev Gastroenterol Hepatol.* 2020;17(9):557-88.
3. Gimple RC, Yang K, Halbert ME, Agnihotri S, and Rich JN. Brain cancer stem cells: resilience through adaptive plasticity and hierarchical heterogeneity. *Nat Rev Cancer.* 2022;22(9):497-514.
4. Wu HJ, and Chu PY. Role of Cancer Stem Cells in Cholangiocarcinoma and Therapeutic Implications. *Int J Mol Sci.* 2019;20(17).
5. Quintana E, Shackleton M, Sabel MS, Fullen DR, Johnson TM, and Morrison SJ. Efficient tumour formation by single human melanoma cells. *Nature.* 2008;456(7222):593-8.
6. Lee TK, Guan XY, and Ma S. Cancer stem cells in hepatocellular carcinoma - from origin to clinical implications. *Nat Rev Gastroenterol Hepatol.* 2022;19(1):26-44.
7. Longo SK, Guo MG, Ji AL, and Khavari PA. Integrating single-cell and spatial transcriptomics to elucidate intercellular tissue dynamics. *Nat Rev Genet.* 2021;22(10):627-44.
8. Song G, Shi Y, Meng L, Ma J, Huang S, Zhang J, et al. Publisher Correction: Single-cell transcriptomic analysis suggests two molecularly distinct subtypes of intrahepatic cholangiocarcinoma. *Nat Commun.* 2022;13(1):2848.
9. Zhang S, Song X, Cao D, Xu Z, Fan B, Che L, et al. Pan-mTOR inhibitor MLN0128 is effective against intrahepatic cholangiocarcinoma in mice. *J Hepatol.* 2017;67(6):1194-203.
10. Chen X, and Calvisi DF. Hydrodynamic transfection for generation of novel mouse models for liver cancer research. *Am J Pathol.* 2014;184(4):912-23.
11. Zhang Y, and Wang X. Targeting the Wnt/beta-catenin signaling pathway in cancer. *J Hematol Oncol.* 2020;13(1):165.
12. Liu J, Qiu J, Zhang Z, Zhou L, Li Y, Ding D, et al. SOX4 maintains the stemness of cancer cells via transcriptionally enhancing HDAC1 revealed by comparative proteomics study. *Cell Biosci.* 2021;11(1):23.
13. Ueharu H, Higuchi M, Nishimura N, Yoshida S, Shibuya S, Sensui K, et al. Expression of Kruppel-like factor 6, KLF6, in rat pituitary stem/progenitor cells and its regulation of the PRRX2 gene. *J Reprod Dev.* 2014;60(4):304-11.
14. Wang H, He L, Li Y, Pu W, Zhang S, Han X, et al. Dual Cre and Dre recombinases mediate synchronized lineage tracing and cell subset ablation in vivo. *J Biol Chem.* 2022;298(6):101965.
15. Bayik D, and Lathia JD. Cancer stem cell-immune cell crosstalk in tumour progression. *Nat Rev Cancer.* 2021;21(8):526-36.
16. Myers KV, Amend SR, and Pienta KJ. Targeting Tyro3, Axl and MerTK (TAM receptors): implications for macrophages in the tumor microenvironment. *Mol*

Cancer. 2019;18(1):94.
17. Holland SJ, Pan A, Franci C, Hu Y, Chang B, Li W, et al. R428, a selective small molecule inhibitor of Axl kinase, blocks tumor spread and prolongs survival in models of metastatic breast cancer. *Cancer Res.* 2010;70(4):1544-54.
18. Halvorsen EC, Hamilton MJ, Young A, Wadsworth BJ, LePard NE, Lee HN, et al. Maraviroc decreases CCL8-mediated migration of CCR5(+) regulatory T cells and reduces metastatic tumor growth in the lungs. *Oncoimmunology.* 2016;5(6):e1150398.
19. Lee Y, Shin JH, Longmire M, Wang H, Kohrt HE, Chang HY, et al. CD44+ Cells in Head and Neck Squamous Cell Carcinoma Suppress T-Cell-Mediated Immunity by Selective Constitutive and Inducible Expression of PD-L1. *Clin Cancer Res.* 2016;22(14):3571-81.
20. Reim F, Dombrowski Y, Ritter C, Buttmann M, Hausler S, Ossadnik M, et al. Immunoselection of breast and ovarian cancer cells with trastuzumab and natural killer cells: selective escape of CD44high/CD24low/HER2low breast cancer stem cells. *Cancer Res.* 2009;69(20):8058-66.
21. Valeta-Magara A, Gadi A, Volta V, Walters B, Arju R, Giashuddin S, et al. Inflammatory Breast Cancer Promotes Development of M2 Tumor-Associated Macrophages and Cancer Mesenchymal Cells through a Complex Chemokine Network. *Cancer Res.* 2019;79(13):3360-71.
22. Cheng K, Cai N, Zhu J, Yang X, Liang H, and Zhang W. Tumor-associated macrophages in liver cancer: From mechanisms to therapy. *Cancer Commun (Lond).* 2022.
23. Allavena P, Digifico E, and Belgiovine C. Macrophages and cancer stem cells: a malevolent alliance. *Mol Med.* 2021;27(1):121.
24. Najafi M, Hashemi Goradel N, Farhood B, Salehi E, Nashtaei MS, Khanlarkhani N, et al. Macrophage polarity in cancer: A review. *J Cell Biochem.* 2019;120(3):2756-65.
25. Goruppi S, Chiaruttini C, Ruaro ME, Varnum B, and Schneider C. Gas6 induces growth, beta-catenin stabilization, and T-cell factor transcriptional activation in contact-inhibited C57 mammary cells. *Mol Cell Biol.* 2001;21(3):902-15.
26. Mansour FA, Al-Mazrou A, Al-Mohanna F, Al-Alwan M, and Ghebeh H. PD-L1 is overexpressed on breast cancer stem cells through notch3/mTOR axis. *Oncoimmunology.* 2020;9(1):1729299.
27. Dianat-Moghadam H, Mahari A, Salahlou R, Khalili M, Azizi M, and Sadeghzadeh H. Immune evader cancer stem cells direct the perspective approaches to cancer immunotherapy. *Stem Cell Res Ther.* 2022;13(1):150.
28. Van Damme H, Dombrecht B, Kiss M, Roose H, Allen E, Van Overmeire E, et al. Therapeutic depletion of CCR8(+) tumor-infiltrating regulatory T cells elicits antitumor immunity and synergizes with anti-PD-1 therapy. *J Immunother Cancer.* 2021;9(2).
29. Han X, Wang Y, Pu W, Huang X, Qiu L, Li Y, et al. Lineage Tracing Reveals the Bipotency of SOX9(+) Hepatocytes during Liver Regeneration. *Stem Cell Reports.* 2019;12(3):624-38.

30. Calvisi DF, Wang C, Ho C, Ladu S, Lee SA, Mattu S, et al. Increased lipogenesis, induced by AKT-mTORC1-RPS6 signaling, promotes development of human hepatocellular carcinoma. *Gastroenterology.* 2011;140(3):1071-83.
31. Qi Y, He J, Zhang Y, Ge Q, Wang Q, Chen L, et al. Heat-inactivated Bifidobacterium adolescentis ameliorates colon senescence through Paneth-like-cell-mediated stem cell activation. *Nat Commun.* 2023;14(1):6121.
32. Ireland L, Luckett T, Schmid MC, and Mielgo A. Blockade of Stromal Gas6 Alters Cancer Cell Plasticity, Activates NK Cells, and Inhibits Pancreatic Cancer Metastasis. *Front Immunol.* 2020;11:297.
33. Hiwatashi K, Tamiya T, Hasegawa E, Fukaya T, Hashimoto M, Kakoi K, et al. Suppression of SOCS3 in macrophages prevents cancer metastasis by modifying macrophage phase and MCP2/CCL8 induction. *Cancer Lett.* 2011;308(2):172-80.
34. Uyanik B, Goloudina AR, Akbarali A, Grigorash BB, Petukhov AV, Singhal S, et al. Inhibition of the DNA damage response phosphatase PPM1D reprograms neutrophils to enhance anti-tumor immune responses. *Nat Commun.* 2021;12(1):3622.
35. Wang T, Xu C, Zhang Z, Wu H, Li X, Zhang Y, et al. Cellular heterogeneity and transcriptomic profiles during intrahepatic cholangiocarcinoma initiation and progression. *Hepatology.* 2022;76(5):1302-17.
36. Zilionis R, Engblom C, Pfirschke C, Savova V, Zemmour D, Saatcioglu HD, et al. Single-Cell Transcriptomics of Human and Mouse Lung Cancers Reveals Conserved Myeloid Populations across Individuals and Species. *Immunity.* 2019;50(5):1317-34 e10.

FIGURE LEGENDS

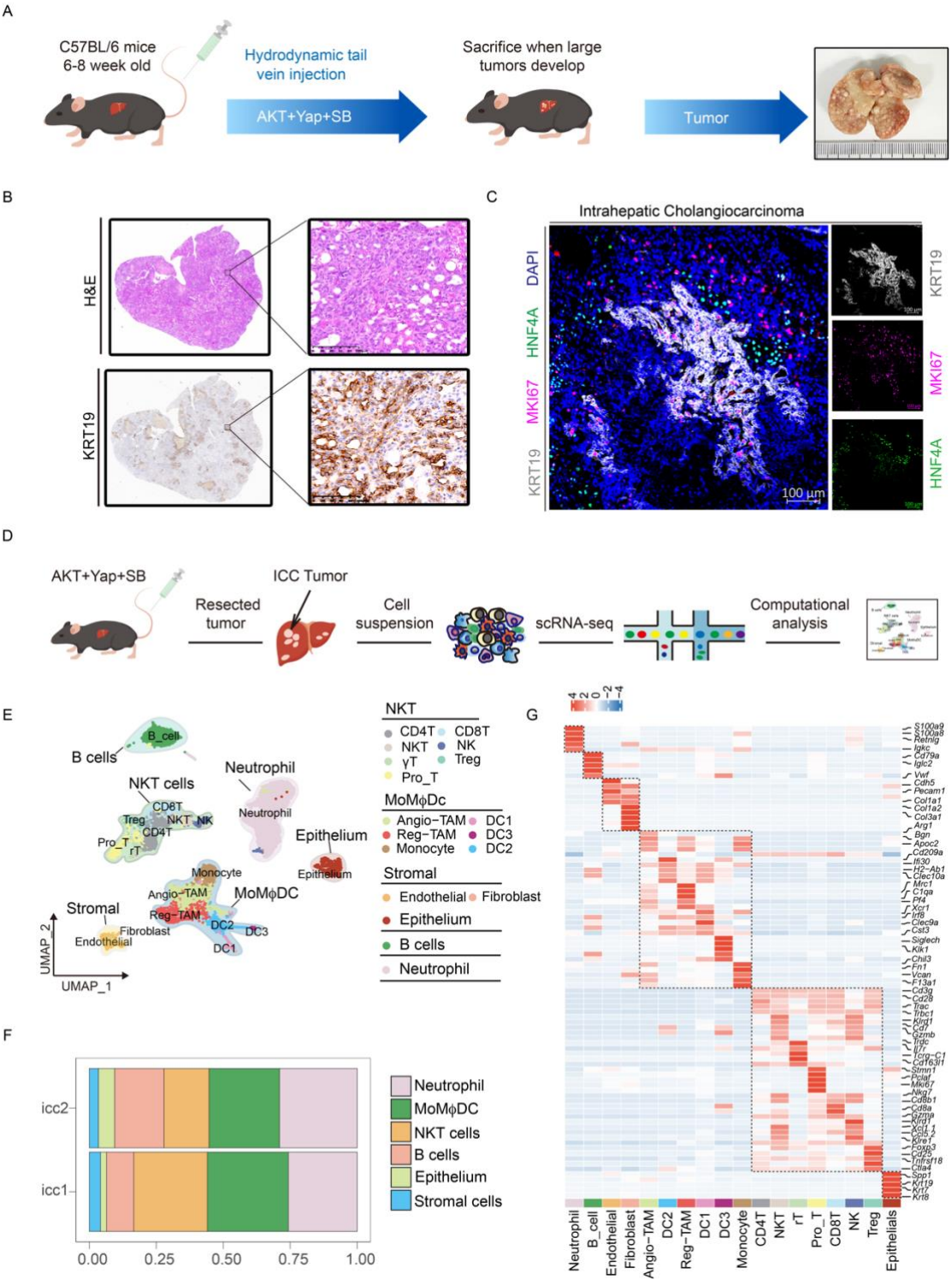

Figure 1. Heterogeneity of cells in mouse ICC sample

A. Schematic of murine ICC induction workflow: (i) Mice were injected with AKT/YAP/SB plasmid via tail vein. (ii) Tumor-bearing mice were sacrificed when large

tumors developed (n = 3).

B. Representative images of H&E and KRT19 IHC staining of liver sections from ICC mice (n = 3 mice). Scale bar, 100μm.

C. Opal/TSA multicolor IF staining with anti-KRT19, MKI67, and HNF4A antibodies; nuclei stained with DAPI (blue) (n = 3 mice). Scale bar, 100μm.

D. Scheme of the workflow for ICC cell isolation and single-cell RNA sequencing.

E. UMAP of single-cell clusters from mice ICC tumor tissues (n = 2), colored by cluster.

F. The proportions of single-cell clusters in each sample.

G. Heatmap of signature genes for eighteen cell clusters.

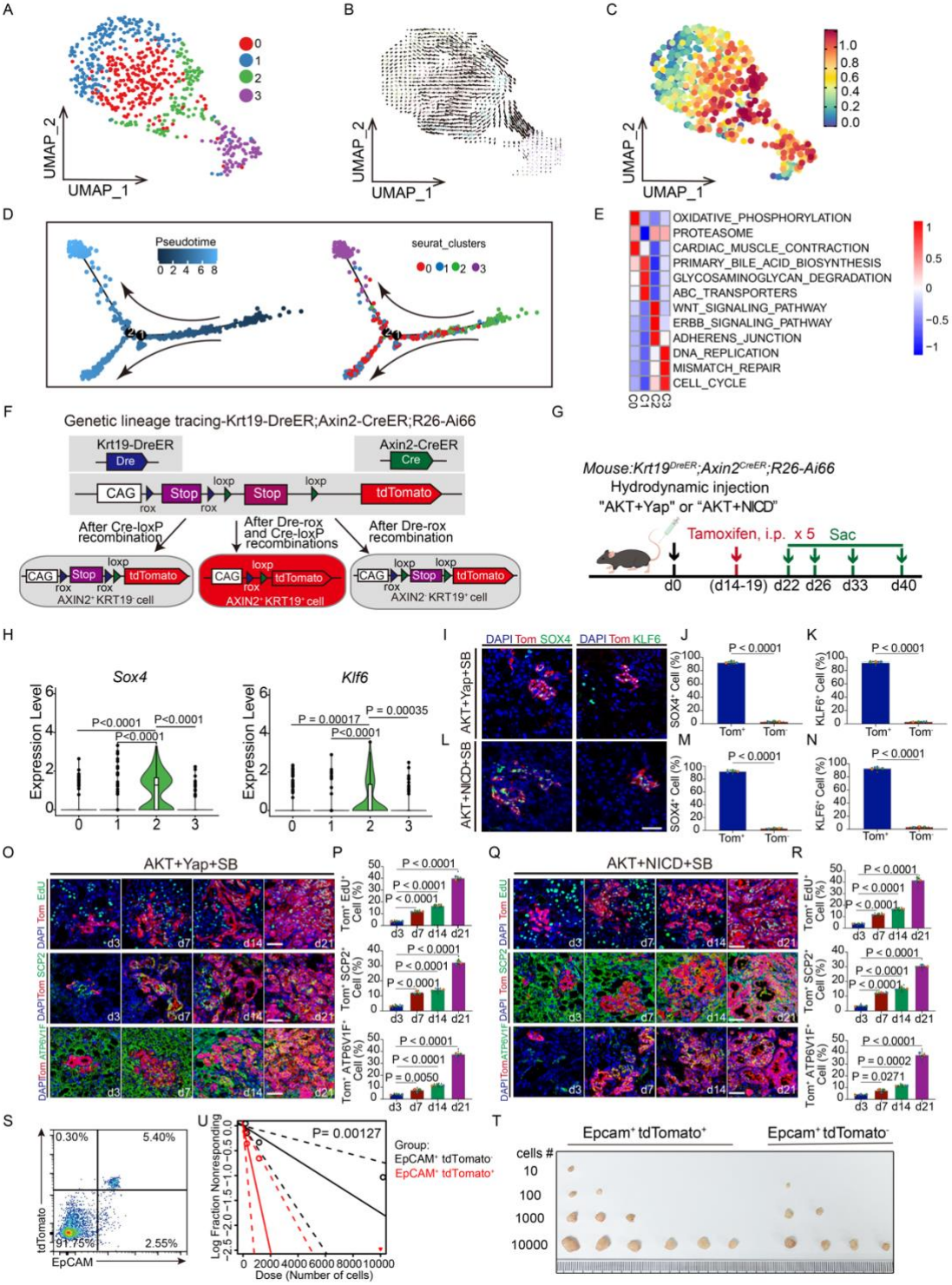

Figure 2 WNT-activated cells are TICs population in mouse ICC

A. UMAP plot showing four epithelial subclusters.

B. Inferred developmental trajectory of epithelial cells by RNA velocity.

C. UMAP plots showing CytoTRACE scores distribution among the epithelial cells.

Higher scores indicate higher stemness.

D. Monocle pseudotime trajectory showing cell differentiation of epithelial cells (left) and four epithelial subclusters (right).

E. Heatmap displaying differential pathways enriched in epithelial cell clusters by GSVA analysis.

F. Schematic diagram of lineage-tracing strategy by *Krt19-DreER* and *Axin2-CreER* system. $AXIN2^+$ $KRT19^+$ cholangiocytes were labeled by dual recombination.

G. Experimental strategies for lineage-tracing of $AXIN2^+$ $KRT19^+$ biliary epithelial cells in ICC mice. Tamoxifen was administered for cell labeling.

H. Violin plot depicts the expression of *Sox4* and *Klf6* among epithelial subclusters. *P* values were calculated by two-tailed unpaired Student's t-test.

I and L. Representative fluorescence images of SOX4 (green) and KLF6 staining (green) and Tom^+ cells (red) in ICC induced by AKT/YAP/SB (I) and AKT/NICD/SB (L). Nuclei are stained with DAPI (blue). Scale bar, 50 μm.

J-K and M-N. Statistical analysis of the $SOX4^+$ (J, M) and $KLF6^+$ (K, N) cells in Tom^+ or Tom^- cells of "AKT+Yap+SB" (J, K) and "AKT+NICD+SB" (M, N) mouse ICC. Error bars represent the mean ± SD from three independent experiments (n = 9 fields from 3 mice). *P* values were calculated by two-tailed unpaired Student's t-test.

O and Q. Representative fluorescence staining for EdU incorporation, SCP2, and ATP6V1F (green) and Tom^+ cells (red) in ICC induced by AKT/Yap/SB (O) and AKT/NICD/SB (Q) after tamoxifen treatment. Nuclei are stained with DAPI (blue). Scale bar, 50 μm.

P and R. Comparison of the percentage of Tom^+EdU^+ cells, Tom^+SCP2^+ cells, and $Tom^+ATP6V1F^+$ cells in ICC induced by AKT/YAP/SB (P) and AKT/NICD/SB (R) for 3 days with 7, 14, and 21 days. Error bars represent mean ± SD from three independent experiments (n = 9 fields from 3 mice). *P* values were calculated by one-way ANOVA Tukey's multiple comparison test.

S. Flow cytometry plots showing $EpCAM^+$/$Tomato^+$ tumor cells were sorted and isolated from ICC tissues.

T. Tumor formation frequency of $EpCAM^+$/Tom^+ and $EpCAM^+$/Tom^- mouse ICC tumor

cell lines in vivo.

U. Analysis of the frequency of primary $EpCAM^+/Tomato^+$ and $EpCAM^+/Tomato^-$ tumor cells forming ICC in vivo. The frequency of allograft development for each cell dosage injected is indicated. *P* value was calculated by the Likelihood ratio test of the single-hit model.

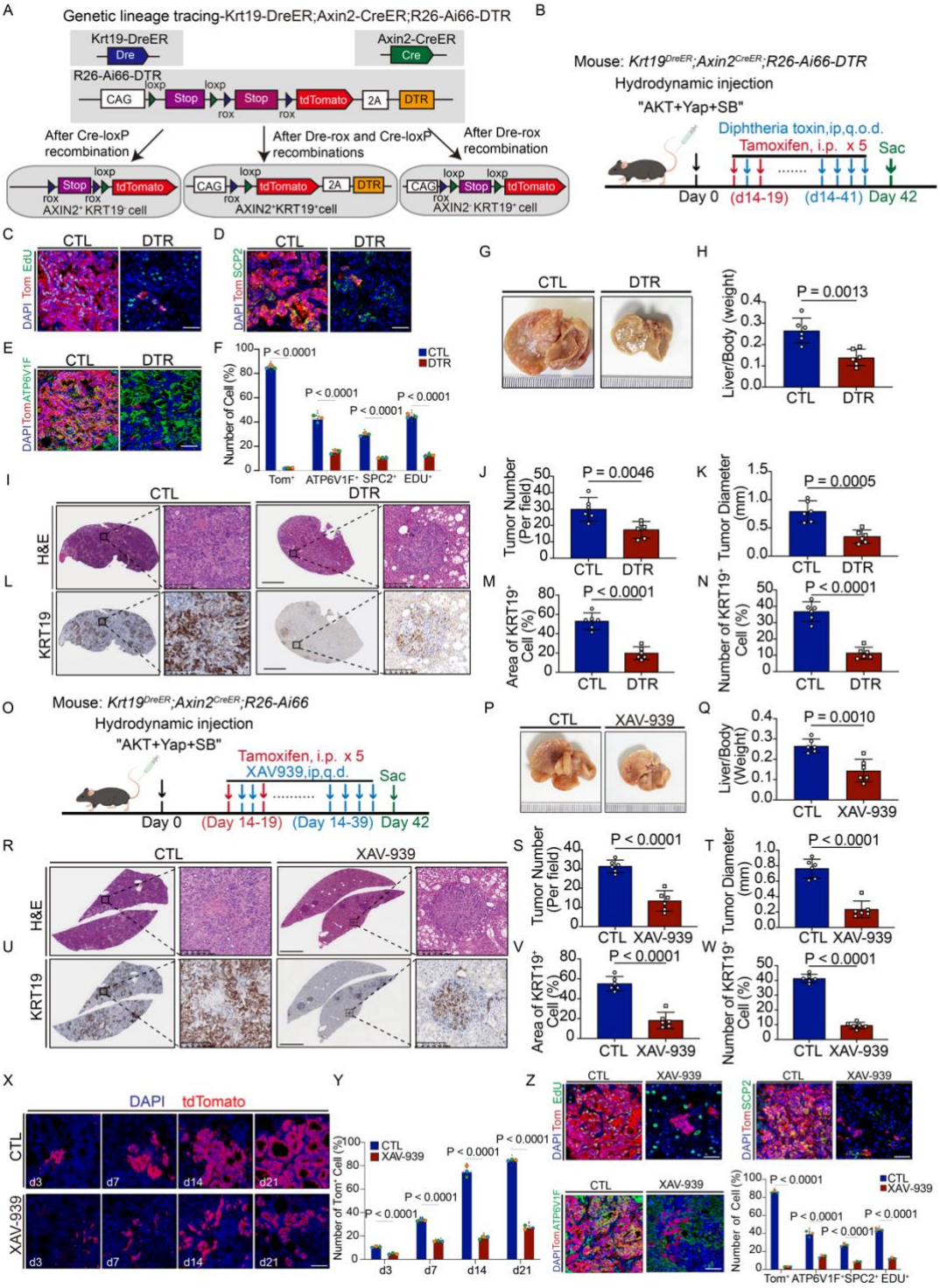

Figure 3. WNT-activated cells and WNT/β-catenin signaling are responsible for mouse ICC progression

A. Schematic diagram of lineage-ablation of KRT19$^+$ AXIN2$^+$ cells by DTR system.

B. Experimental strategies for lineage-ablation of KRT19$^+$ AXIN2$^+$ cells of ICC in *Krt19-DreER*; *Axin2-CreER*; *R26-Ai66-DTR* mice. KRT19$^+$ AXIN2$^+$ cells were ablated

after tamoxifen and diphtheria toxin were given.

C-E. Fluorescence staining for EdU incorporation (C), SCP2 (D), and ATP6V1F (E) (green) and Tom^+ cells (red) from ICC-induced mice after diphtheria toxin treatment. Scale bar, 50 μm.

F. Quantification of the number of Tom^+ cells, Tom^+ EdU^+ cells, Tom^+ $SCP2^+$ cells, and Tom^+ $ATP6V1F^+$ cells in ICC after diphtheria toxin treatment. Error bars are mean ± SD from three independent experiments (n = 9 fields from 3 mice). *P* values were calculated by two-tailed unpaired Student's t-test.

G. Representative images of whole liver morphology after diphtheria toxin treatment.

H. Statistical analysis of liver to body weight ratio after diphtheria toxin treatment. Values are mean ± SD (n = 6 mice). *P* value was calculated by two-tailed unpaired Student's t-test.

I-N. Representative images of H&E (I) and KRT19 staining (L) of liver sections from ICC-induced mice after tamoxifen and diphtheria toxin treatment, with scale bars of 200 μm. Statistical analyses include ICC number (J), ICC diameter (K), KRT19 area (M), and $KRT19^+$ cell number (N). Error bars are mean ± SD from six independent biological replicates (n = 6 mice). *P* values were calculated by two-tailed unpaired Student's t-test.

O. Experimental strategies for XAV-939 treatment of ICC in *Krt19-DreER*; *Axin2-CreER*; *R26-Ai66* and WT mice.

P. Representative image of whole liver morphology after XAV-939 treatment.

Q. Statistical analysis of liver to body weight ratio after XAV-939 treatment. Error bars are mean ± SD from six independent biological replicates (n = 6 mice). *P* value was calculated by two-tailed unpaired Student's t-test.

R-W. Representative images of H&E (R) and KRT19 staining (U) of liver sections from ICC-induced mice after XAV-939 treatment, with scale bars of 200 μm. Statistical analyses include ICC number (S), ICC diameter (T), KRT19 area (V), and $KRT19^+$ cell number (W). Error bars are mean ± SD from six independent biological replicates (n = 6 mice). *P* values were calculated by two-tailed unpaired Student's t-test.

X-Y. Fluorescence images of lineage tracing at days 3, 7, 14, and 21 in ICC after XAV-

939 treatment, with nuclei stained with DAPI (blue) and a scale bar of 50 μm (X). Statistical analysis of the number of Tom^+ cells at these time points (Y) shows error bars representing mean ± SD from three independent experiments (n = 9 fields from 3 mice). *P* values were calculated by two-tailed unpaired Student's t-test.

Z. Fluorescence staining for EdU (green) incorporation, SCP2 (green), and ATP6V1F (green) and Tom^+ cells (red) from ICC-induced mice after XAV-939 treatment. Scale bar, 50 μm. Quantification of the number of Tom^+ cells, EdU^+ cells, $SCP2^+$ cells, and $ATP6V1F^+$ cells in ICC after XAV-939 treatment (bottom right). Error bars are mean ± SD from three independent experiments (n = 9 fields from 3 mice). *P* values were calculated by two-tailed unpaired Student's t-test.

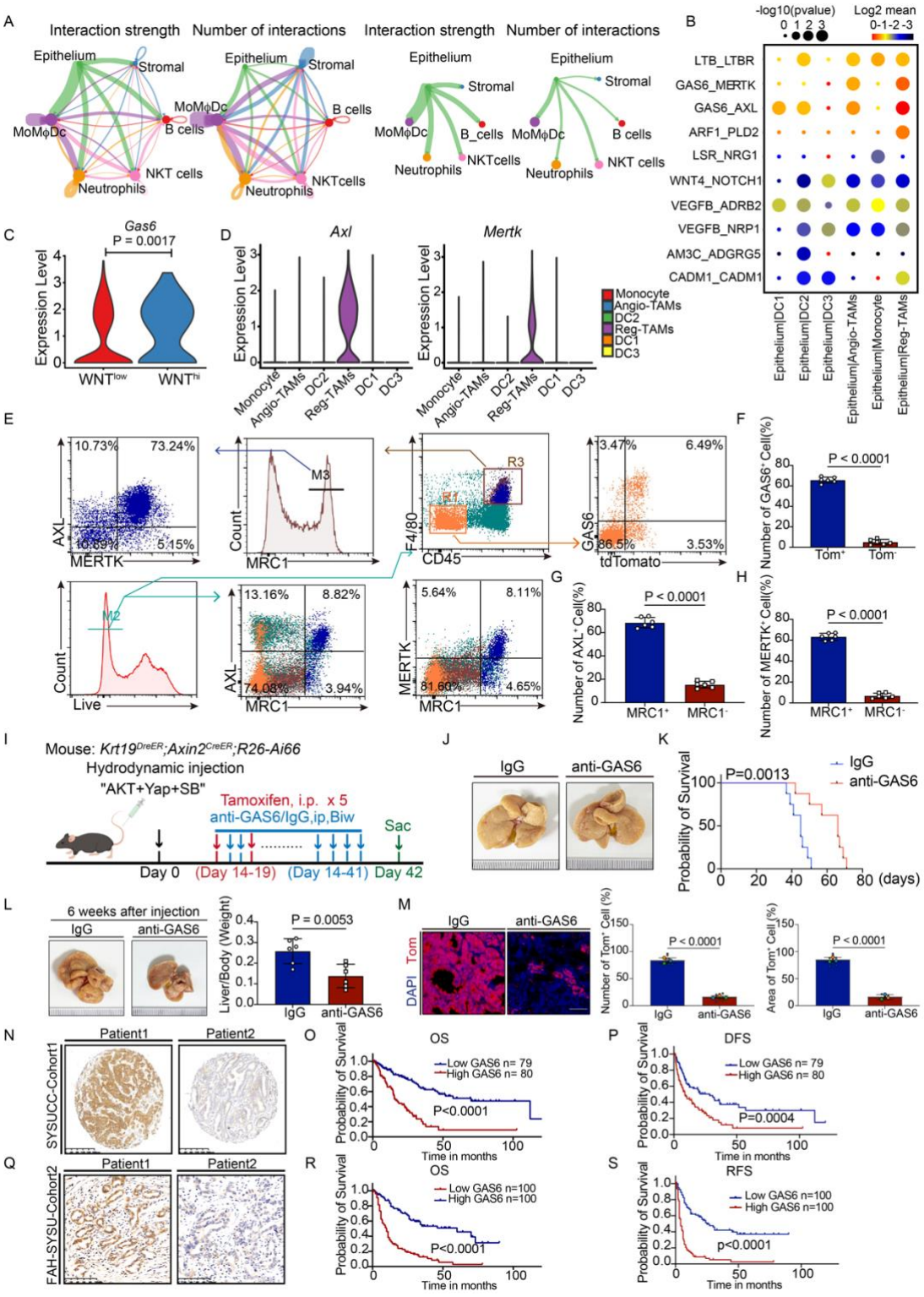

Figure 4. GAS6 is highly expressed and plays an important role in TIC maintenance in the ICC

A. Circle plots show the interaction strength and number of interactions in the cell-cell communication network among the six major clusters (left) analyzed by CellChat. The

cell-cell communication network between epithelium and other cell types was presented (right). The line width indicates the communication probability.

B. Dot plots depict the significance ($-\log_{10}$ P value) and strength (Log_2 mean value) of detail ligand-receptor pairs between epithelium and other cell types analyzed by CellphoneDB.

C. Violin plot depicts the expression of Gas6 between the WNT^{hi} epithelial subcluster and WNT^{low} epithelial subclusters. *P* values were calculated by two-tailed unpaired Student's t-test.

D. Violin plot depicts the expression of *Axl* and *Mertk* in MoMϕDC subclusters.

E-H. Representative flow plots (E) and corresponding graphs show Tom^+ $GAS6^+$ tumor-infiltrating cells and the levels of $MRC1^+/MERTK^+/AXL^+$ in infiltrating Reg-TAM. Statistical analysis of $GAS6^+$ cells in Tom^+ cells or Tom^- cells of mouse ICC (F), statistical analysis of AXL^+ cells in $MRC1^+$ or $MRC1^-$ cells in ICC (G), and statistical analysis of $MERTK^+$ cells in $MRC1^+$ or $MRC1^-$ cells in mouse ICC (H). Error bars represent mean ± SD from six independent experiments (n = 6 mice). *P* values were calculated by two-tailed unpaired Student's t-test.

I. Experimental strategies for the anti-GAS6 treatment of ICC in *Krt19-DreER*; *Axin2-CreER*; *R26-Ai66* and WT mice. The mice were sacrificed when large tumors developed or six weeks after the plasmids were injected.

J. Representative image of whole liver morphology after anti-GAS6 treatment or IgG treatment. The time of mice developed lethal tumor burden was shown.

K. The Kaplan-Meier overall survival curve of mice of ICC after anti-GAS6 treatment or IgG treatment. *P* value was calculated by log-rank test.

L. Representative image of whole liver morphology after treated with anti-GAS6 or IgG for six weeks (left). Statistical analysis of liver to body weight ratio after treated with anti-GAS6 or IgG for six weeks (right). Error bars are mean ± SD from six independent biological replicates (n = 6 mice). *P* value was calculated by two-tailed unpaired Student's t-test.

M. Representative fluorescence images of lineage tracing (left), statistical analysis of the number of Tom^+ cells (middle), and statistical analysis of the area of Tom^+ cells

(right) in mouse ICC after anti-GAS6 treatment or IgG treatment. Scale bar, 50 μm. Error bars are mean ± SD from three independent experiments (n = 9 fields from 3 mice). *P* values were calculated by two-tailed unpaired Student's t-test.

N. Representative images of GAS6 staining of human ICC tissue array from SYSUCC cohort1. Representative images of high GAS6 expression and low GAS6 expression were shown. Scale bar, 200μm.

O and P. Kaplan-Meier survival curves were established by GAS6 expression. Patients with ICC were divided into high- and low-expression groups based on GAS6 expression. Overall survival (OS, O) and disease-free survival (DFS, P) of SYSUCC cohort1 are shown. *P* values were calculated by log-rank test.

Q. Representative images of GAS6 staining of human ICC tissues from FAH-SYSU cohort2. Representative images of high GAS6 expression and low GAS6 expression were shown. Scale bar, 100μm.

R and S. Kaplan-Meier survival curves were established by GAS6 expression. Patients with ICC were divided into high- and low-expression groups based on GAS6 expression. OS (R) and recurrence-free survival (RFS, S) of FAH-SYSU cohort2 are shown. *P* values were calculated by log-rank test.

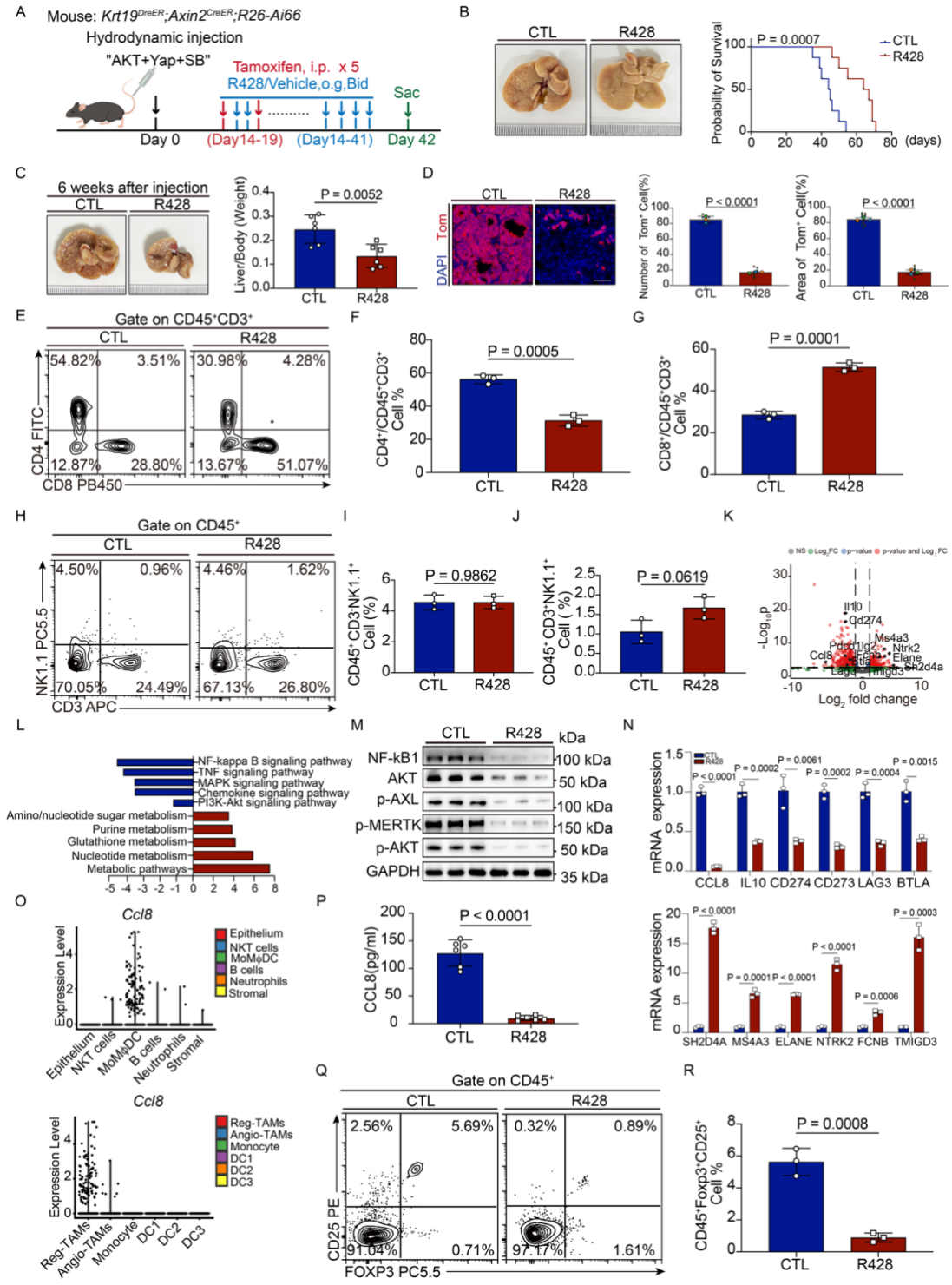

Figure 5. Inhibition of AXL/MERTK suppressed ICC progression and Treg numbers

A. Experimental strategies for R428 treatment in *Krt19-DreER*; *Axin2-CreER*; *R26-Ai66* mice. The mice were sacrificed when large tumors developed.

B. Representative image of whole liver morphology after R428 treatment (left). The time of mice developed lethal tumor burden was shown. The Kaplan-Meier overall

survival curve of mice of ICC after R428 treatment (right). *P* value was calculated by log-rank test.

C. Representative image of whole liver morphology after R428 treatment for six weeks (left). Statistical analysis of liver to body weight ratio after R428 treatment (right). Error bars are mean ± SD from six independent biological replicates (n = 6 mice). *P* value was calculated by two-tailed unpaired Student's t-test.

D. Representative fluorescence images of lineage tracing after R428 treatment (left). Scale bar, 50 μm. Statistical analysis of the number (middle) and area (right) of Tom^+ cells after R428 treatment. Values are mean ± SD from three independent experiments (n = 9 fields from 3 mice). *P* values were calculated by two-tailed unpaired Student's t-test.

E-G. Representative flow plots (E) and corresponding graphs of the frequency of tumor-infiltrating $CD4^+$ (F), and $CD8^+$ (G) T cells after R428 treatment. Values are mean ± SD from three independent experiments (n = 3 mice). *P* values were calculated by two-tailed unpaired Student's t-test.

H-J. Representative flow plots (H) and corresponding graphs of the frequency of tumor-infiltrating NK cells (I) and NKT cells (J) after R428 treatment. Error bars are mean ± SD from three independent experiments (n = 3 mice). *P* values were calculated by two-tailed unpaired Student's t-test.

K. Volcano plot showing differentially expressed genes between R428 treatment and vehicle treatment mouse ICC Reg-TAMs. The genes passed p-value and fold change thresholds (p-value< 0.01; fold change ⩾2 or ⩽-2) were shown in red.

L. KEGG pathway analysis of the up- and down-regulated differentially expressed genes in ICC tumor cells after R428 treatment.

M. Western blotting analysis of NF-kB1, AKT, p-AXL, p-MERTK, p-AKT, and GAPDH in ICC Reg-TAMs after R428 treatment.

N. The qPCR analysis of the expression of differentially expressed genes in ICC tumor cells after R428 treatment. Values are mean ± SD from three independent experiments (n = 3 mice). *P* values were calculated by two-tailed unpaired Student's t-test.

O. Violin plot showing Ccl8 was specifically expressed in the MoMϕDC cluster (top). Violin plot depicts the specific expression of Ccl8 in Reg-TAMs (bottom).

P. ELISA showed the protein levels of CCL8 in ICC Reg-TAMs tissues between R428 treatment and vehicle treatment groups. Values are mean ± SD from six independent biological replicates (n = 6 mice). *P* value was calculated by two-tailed unpaired Student's t-test.

Q and R. Representative flow plots (Q) and corresponding graph of the frequency of tumor-infiltrating Tregs (R) after R428 treatment. Values are mean ± SD from three independent experiments (n = 3 mice). *P* value was calculated by two-tailed unpaired Student's t-test.

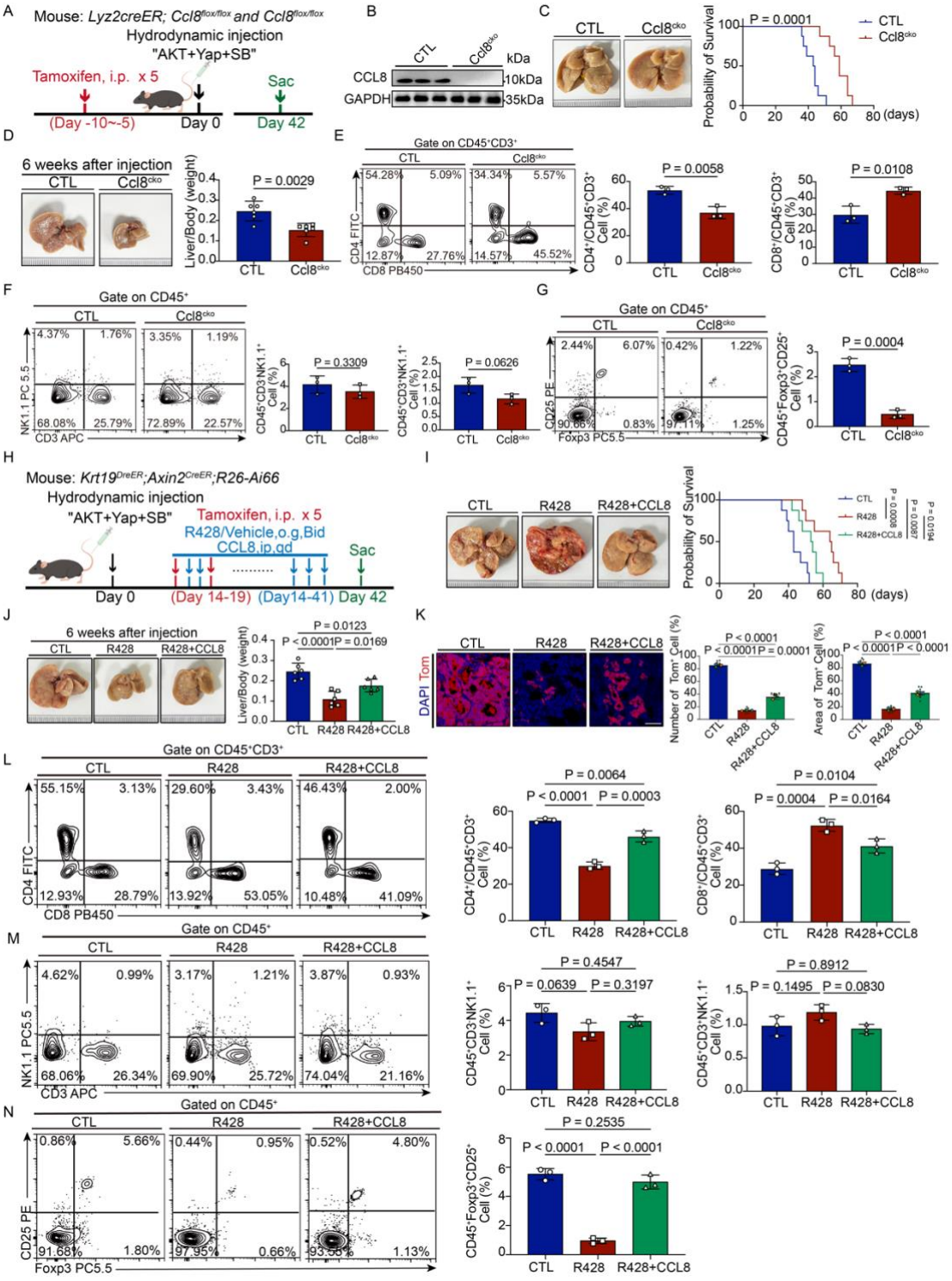

Figure 6. CCL8 is the downstream mediator of AXL/MERTK signaling in Reg-TAMs

A. Experimental design for induction of ICC in *Lyz2-CreER* (Control group) and *Lyz2-CreER; Ccl8$^{flox/flox}$* (Ccl8^{cko} group) mice. The mice were sacrificed when large tumors developed or six weeks after the plasmids were injected.

B. The knockout efficiency of CCL8 in Lyz2^{+} cells was validated by Western blot

analysis.

C. Representative image of whole liver morphology in control and $Ccl8^{cko}$ mice (left). The time of mice developed lethal tumor burden was shown. The Kaplan-Meier overall survival curve of Control and $Ccl8^{cko}$ mice (right). *P* value was calculated by log-rank test.

D. Representative image of whole liver morphology in Control and $Ccl8^{cko}$ mice with the plasmid injected for six weeks (left). Statistical analysis of liver to body weight ratio in control and $Ccl8^{cko}$ mice (right). Values are mean ± SD from six independent biological replicates (n = 6 mice). *P* value was calculated by two-tailed unpaired Student's t-test.

E. Representative flow plot showing the frequency of $CD4^+$ and $CD8^+$ T cells in control and $Ccl8^{cko}$ mice (left). Statistical analysis of the number of $CD4^+$ (left) and $CD8^+$ (right) T cells in control and $Ccl8^{cko}$ mice (right). Values are mean ± SD from three independent experiments (n = 3 mice). *P* values were calculated by two-tailed unpaired Student's t-test.

F. Representative flow plot showing the frequency of NK and NKT cells in control and $Ccl8^{cko}$ mice (left). Statistical analysis of the number of NK and NKT cells in control and $Ccl8^{cko}$ mice (right). Values are mean ± SD from three independent experiments (n = 3 mice). *P* values were calculated by two-tailed unpaired Student's t-test.

G. Representative flow plot showing the frequency of $CD25^+$ $Foxp3^+$ cells in control and $Ccl8^{cko}$ mice (left). Statistical analysis of the number of $CD25^+$ $Foxp3^+$ cells in control and $Ccl8^{cko}$ mice (right). Values are mean ± SD from three independent experiments (n = 3 mice). *P* value was calculated by Student's t-test.

H. Experimental strategies for R428 treatment or R428 treatment with CCL8 (R428+CCL8) of ICC in *Krt19-DreER*; *Axin2-CreER*; *R26-Ai66* and WT mice. The mice were sacrificed when large tumors developed or six weeks after the plasmids were injected.

I. Representative image of whole liver morphology in different treatment groups. The time of mice developed lethal tumor burden was shown. The Kaplan-Meier overall survival curve of mice of ICC in different treatment groups. *P* value was calculated by

log-rank test.

J. Representative image of whole liver morphology in different treatment groups (mice were treated for six weeks). Statistical analysis of liver to body weight ratio in different treatment groups. Values are mean ± SD from six independent biological replicates (n = 6 mice). *P* values were calculated by one-way ANOVA with Tukey's multiple comparison test.

K. Representative fluorescence images of lineage tracing in different treatment groups. Scale bar, 50 μm. Statistical analysis of the number (middle) and area (right) of Tom^+ cells in different treatment groups. Values are mean ± SD from six independent biological replicates (n = 9 fields from 3 mice). *P* values were calculated by one-way ANOVA with Tukey's multiple comparison test.

L. Representative flow plots and corresponding graphs of the frequency of tumor-infiltrating $CD4^+$ and $CD8^+$ T cells after R428 or R428+CCL8 treatment. Values are mean ± SD from three independent experiments (n = 3 mice). *P* values were calculated by one-way ANOVA with Tukey's multiple comparison test.

M. Representative flow plots and corresponding graph of the frequency of tumor-infiltrating NK and NKT cells after R428 or R428+CCL8 treatment. Values are mean ± SD from three independent experiments (n = 3 mice). *P* values were calculated by one-way ANOVA with Tukey's multiple comparison test.

N. Representative flow plots and corresponding graph of the frequency of tumor-infiltrating $CD25^+Foxp3^+$ Tregs after R428 or R428+CCL8 treatment. Values are mean ± SD from three independent experiments (n = 3 mice). *P* values were calculated by one-way ANOVA with Tukey's multiple comparison test.

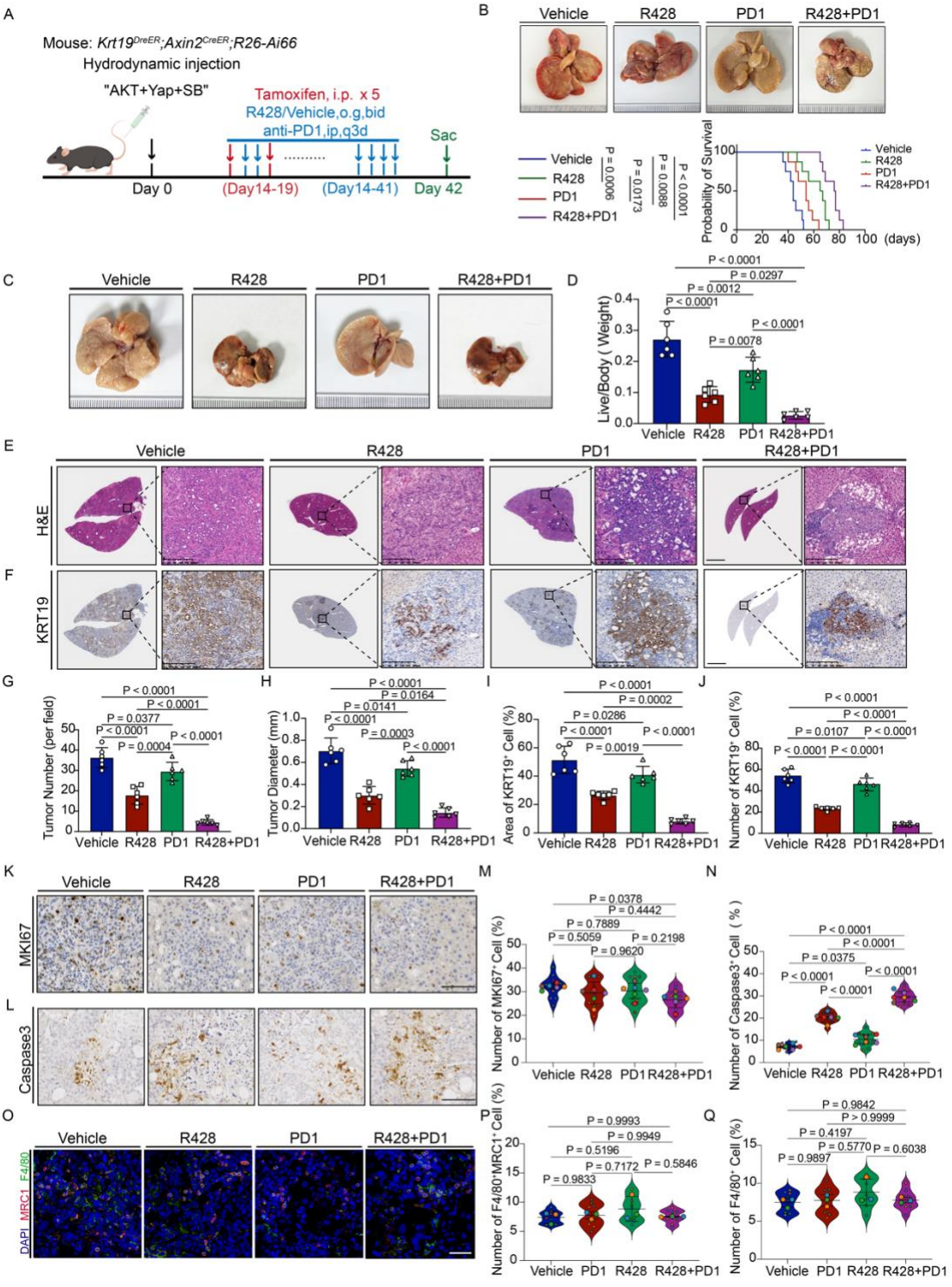

Figure 7. R428 treatment sensitizes murine ICC cells to anti-PD-1 treatment

A. Experimental strategies for ICC mice with treatment as indicated. The mice were sacrificed when large tumors developed.

B. Representative image of whole liver morphology from ICC mice with treatment as indicated (upper). The time of mice developed lethal tumor burden was shown. The

Kaplan-Meier overall survival curve of mice of ICC with treatment as indicated (lower). *P* values were calculated by log-rank test.

C and D. Representative image of whole liver morphology from ICC mice with treatment as indicated. Statistical analysis of liver to body weight ratio from ICC mice with treatment as indicated (right). Values are mean ± SD from six independent biological replicates (n = 6 mice). ns, not significant, *P* values were calculated by one-way ANOVA with Tukey's multiple comparison test.

E-J. Representative images of H&E (E) and KRT19 (F) staining of liver sections from ICC mice under different treatments (upper), with scale bars of 200 μm. Statistical analyses of ICC number (G), ICC diameter (H), KRT19 area (I), and $KRT19^+$ cells (J) in different treatment groups. Values represent mean ± SD from six independent biological replicates (n = 6 mice). *P* values were calculated by one-way ANOVA with Tukey's multiple comparison test.

K-N. Representative images of MKI67 (K) and active-Caspase3 (L) staining of liver sections from ICC mice under indicated treatments, with scale bars of 100 μm. Statistical analyses of $MKI67^+$ cells (M) and active-$Caspase3^+$ cells (N) were performed. Values represent mean ± SD from six independent biological replicates (n = 12 fields from 6 mice). *P* values were calculated by one-way ANOVA with Tukey's multiple comparison test.

O-Q. Fluorescence staining for F4/80 (green) and MRC1 (red) of liver sections from ICC mice under indicated treatments, with scale bars of 50 μm (O). Statistical analyses of $F4/80^+MRC1^+$ cells and $F4/80^+$ cells (P, Q) were performed. Error bars represent mean ± SD from three independent experiments (n = 9 fields from 3 mice). *P* values were calculated by one-way ANOVA with Tukey's multiple comparison test.

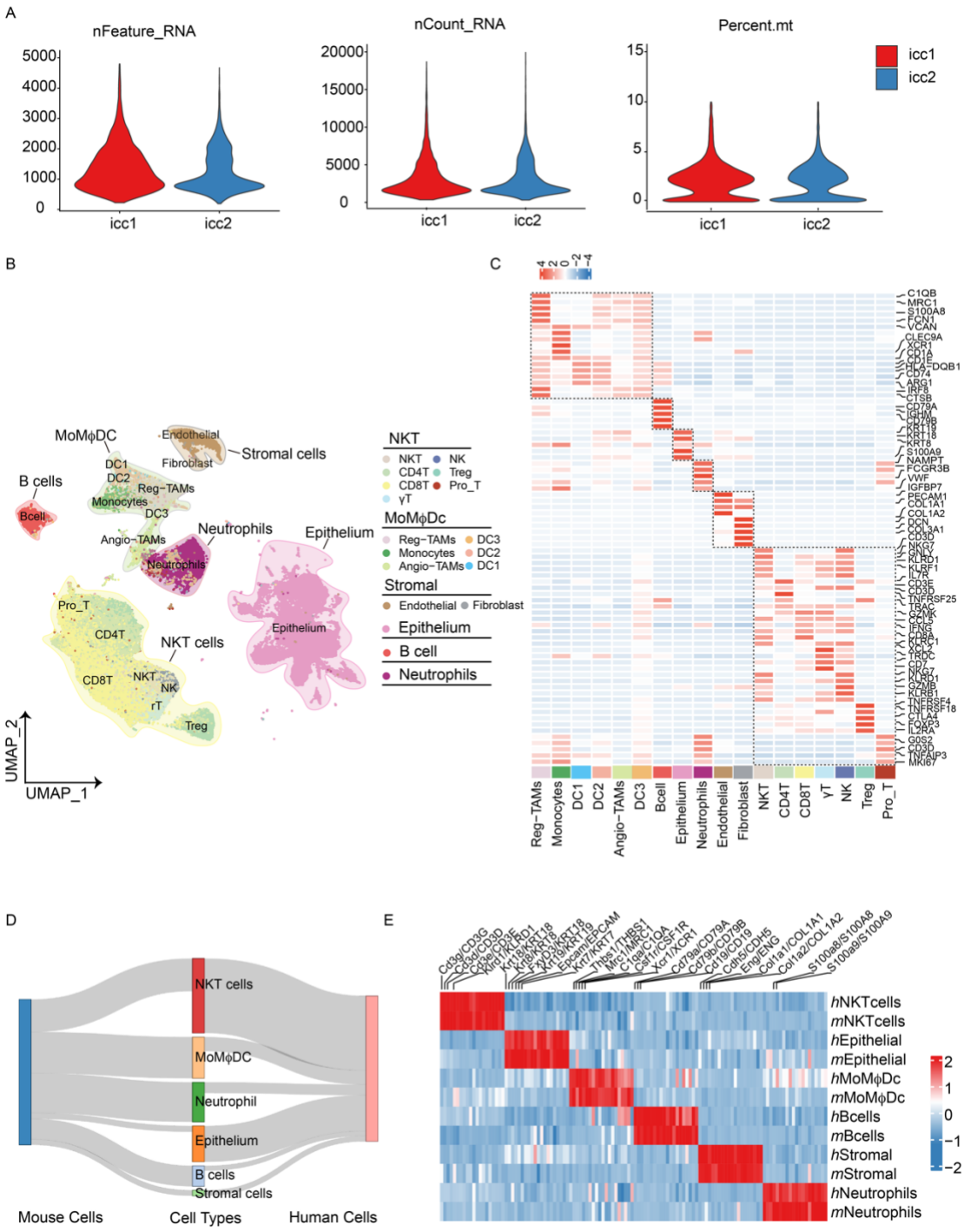

Figure S1, Related to Figure 1. Mouse and human ICC contain a similar cellular composition and conserved gene signatures within the same cell type

A. Violin plots of the number of genes, total number of RNA reads, and percentage of mitochondrial genes per cell in each sample.

B. UMAP of single-cell clusters from human ICC tumor tissues, colored by cell cluster.

C. Heatmap of signature genes for eighteen cell clusters.

D. Sankey diagram represents the contribution of the mouse cells and human cells to the six major groups.

E. Heatmap of six major groups showing genes similarly enriched within mouse and human cell clusters from mice ICC tumor tissues and human ICC tumor tissues.

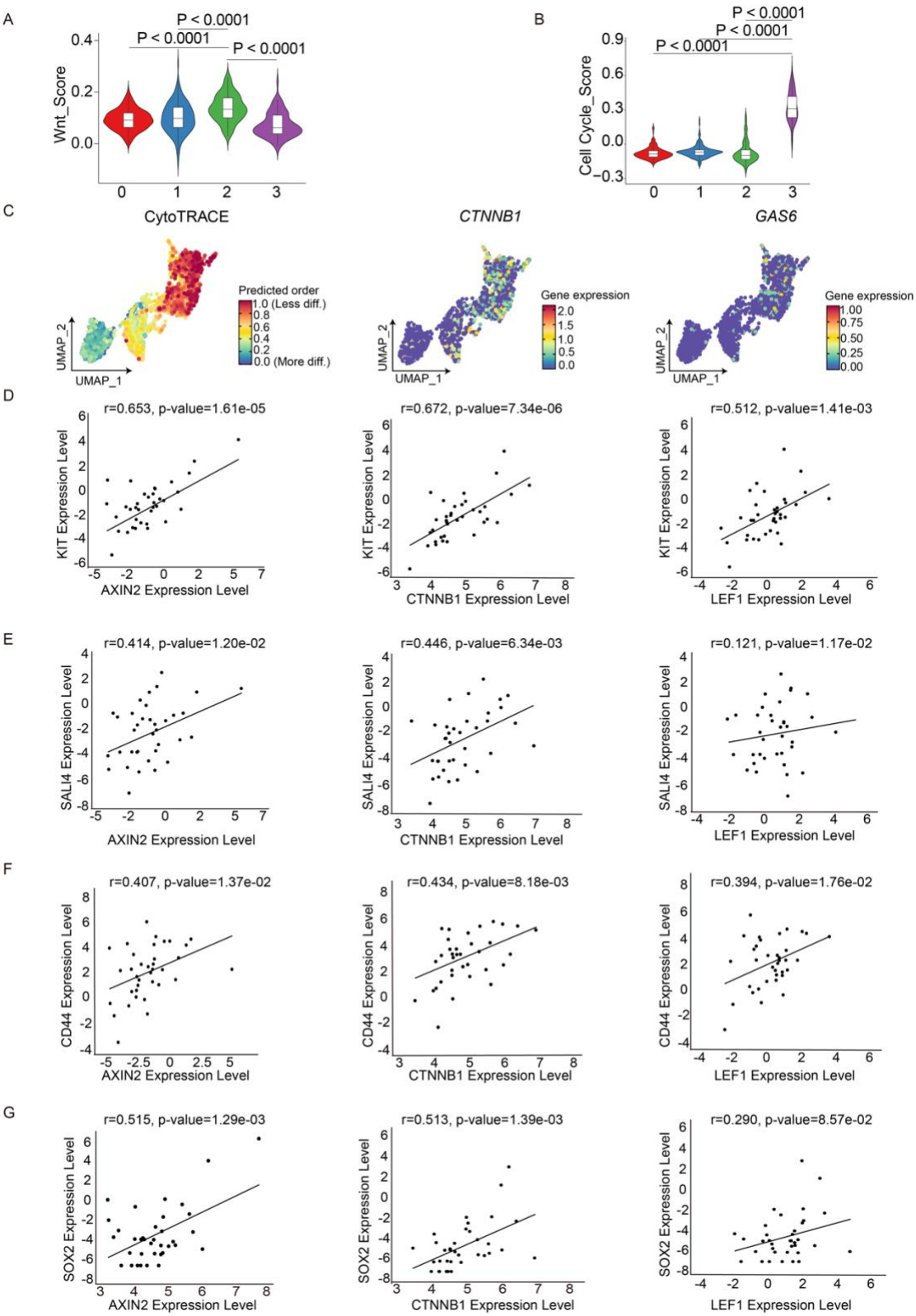

Figure S2, Related to Figure 2. WNT/β-catenin signaling is enriched in the TICs of mouse and human ICC samples

A. Violin plot depicts WNT pathway score among four epithelial subclusters. *P* values

were calculated by a non-parametric Wilcoxon test.

B. Violin plot depicts cell cycle pathway score among four epithelial subclusters. *P* values were calculated by non-parametric Wilcoxon test.

C. UMAP plots showing the CytoTRACE scores distribution among the epithelial cells from one representative human ICC sample (left). Feature plots of *CTNNB1* (middle) and *GAS6* (right) gene expression in the epithelial cells in the human ICC sample.

D-G. Correlation between *KIT* (D), *SALL4* (E), *CD44* (F), *SOX2* (G), and canonical WNT/β-catenin signaling pathway genes (*AXIN2*, *CTNNB1*, and *LEF1*) were analyzed by Pearson's correlation test according to the TCGA-CHOL datasets.

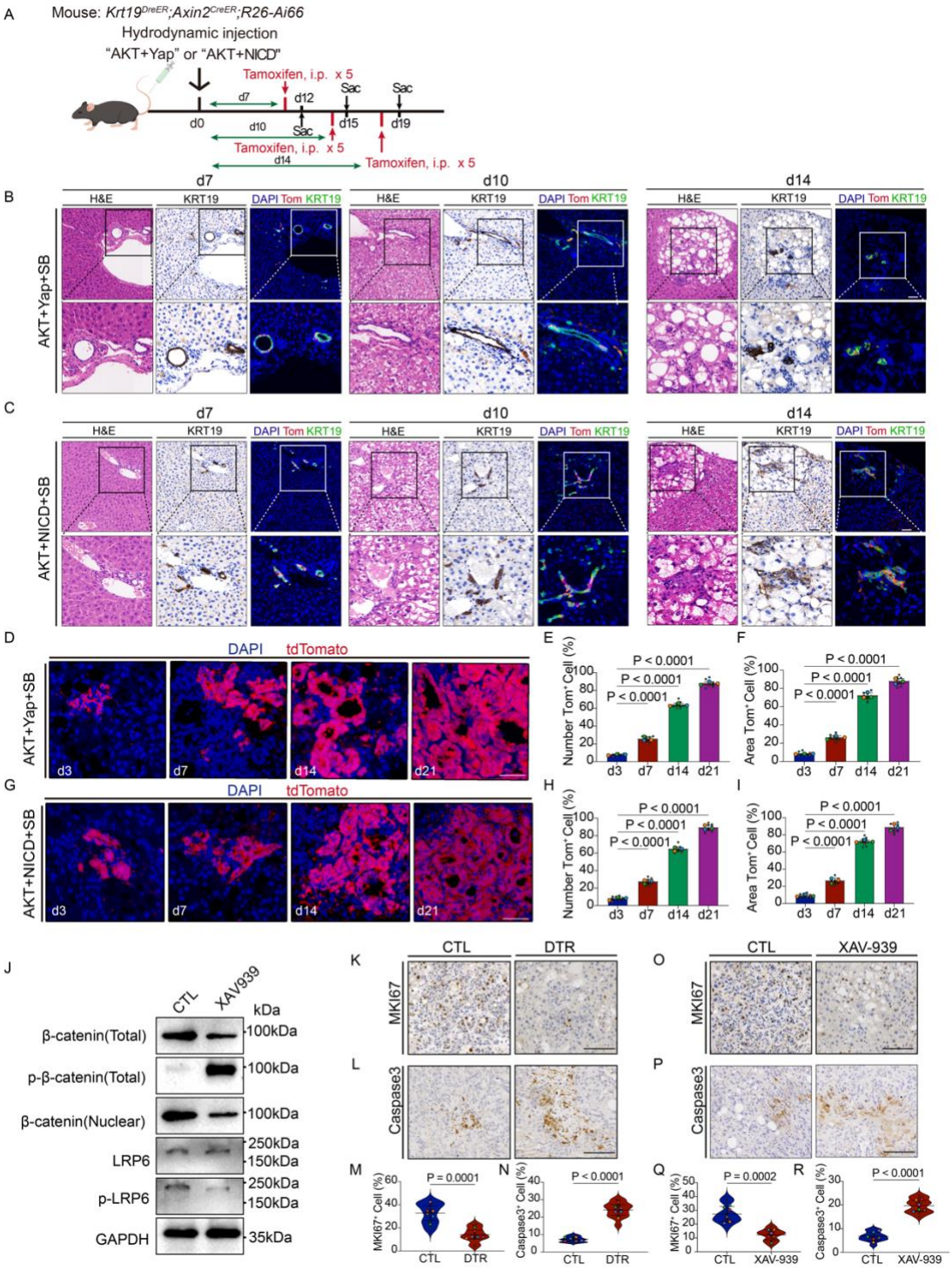

Figure S3, Related to Figure 2. WNT-activated cells and WNT/β-catenin signaling are responsible for mouse ICC progression

A. Experimental strategies for lineage-tracing of KRT19^{+} AXIN2^{+} cells of ICC in *Krt19-DreER; Axin2-CreER; R26-Ai66-DTR* mice. KRT19^{+} AXIN2^{+} cells were labeled after tamoxifen were given.

B-C. Representative images of H&E staining, KRT19 IHC staining, and KRT19 and RFP IF staining at days 7, 10, and 14 in ICC after AKT/YAP/SB treatment (B) and AKT/NICD/SB treatment (C). Nuclei are stained with DAPI (blue). Scale bar, 50 μm.

D-I. Fluorescence images of lineage tracing in ICC induced by AKT/YAP/SB (D) and AKT/NICD/SB (G) after tamoxifen treatment. Nuclei are stained with DAPI (blue). Scale bar, 50 μm. Comparisons of the number (E, H) and area (F, I) of Tom^+ cells in ICC for 3, 7, 14, and 21 days after AKT/YAP/SB or AKT/NICD/SB treatment. Error bars represent mean ± SD from three independent experiments (n = 9 fields from 3 mice). *P* values were calculated by one-way ANOVA with Tukey's multiple comparison test.

J. Western blotting analysis of β-catenin (Total), p-β-catenin (Total), β-catenin (Nuclear), LRP6, p-LRP6, and GAPDH in ICC TICs after XAV-939 treatment.

K and L. Representative image of MKI67 (K) and active-Caspase3 (L) staining of liver sections from ICC-induced mice after diphtheria toxin treatment. Scale bar, 100μm.

M and N. Statistical analysis of $MKI67^+$ (M) and active-$Caspase3^+$ (N) cells after diphtheria toxin treatment. Values are mean ± SD from six independent biological replicates (n = 12 fields from 6 mice). *P* values were calculated by two-tailed unpaired Student's t-test.

O and P. Representative image of MKI67 (O) and active-Caspase3 (P) staining of liver sections from ICC-induced mice after XAV-939 treatment. Scale bar, 100μm.

Q and R. Statistical analysis of $MKI67^+$ (Q) and active-$Caspase3^+$ (R) cells after XAV-939 treatment. Values are mean ± SD from six independent biological replicates (n = 12 fields from 6 mice). *P* values were calculated by two-tailed unpaired Student's t-test.

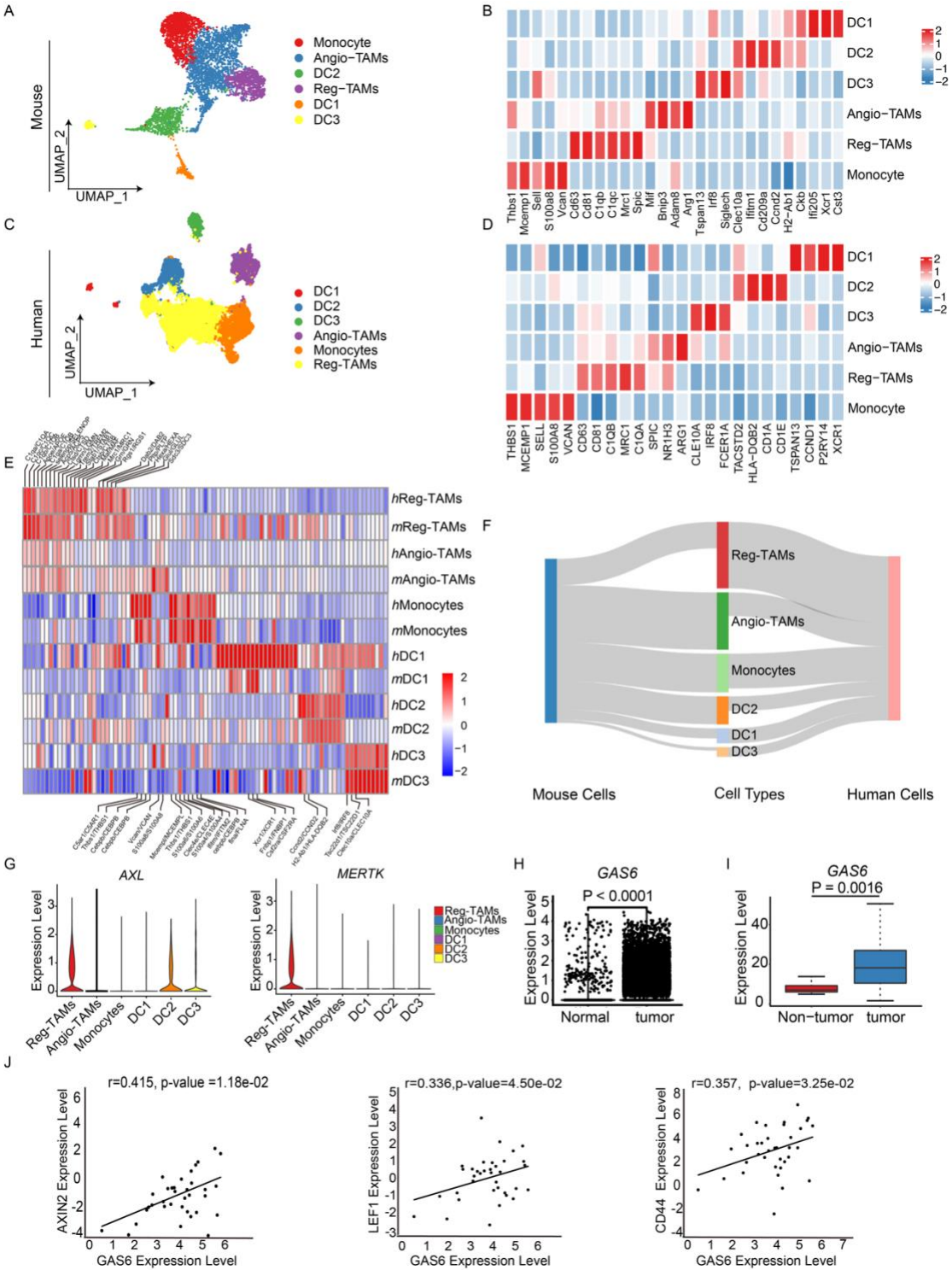

Figure S4, Related to Figure 4. Expression of GAS6-AXL/MERTK in human ICC samples

A-D. UMAP of myeloid cell clusters from mouse (A) and human (C) ICC tumor tissues, colored by cell cluster. Heatmap of signature genes for myeloid cell clusters from mouse (B) and human (D) ICC tumor tissues, with each cell cluster represented by

specifically expressed genes.

E. Heatmap showing genes similarly enriched within mouse and human myeloid cell clusters in ICC tumor tissues.

F. Sankey diagram represents the contribution of the mouse cells and human cells to the myeloid cell clusters.

G. Violin plot depicts the expression of *AXL* and *MERTK* in myeloid cell clusters from human ICC tumor tissues.

H. Violin plot depicts expression of *GAS6* in normal and ICC tumor cells according to human ICC scRNAseq datasets. *P* value was calculated by two-tailed unpaired Student's t-test.

I. Expression of *GAS6* mRNA is higher in human non-tumor control compared with ICC tissues according to the TCGA-CHOL datasets. *P* value was calculated by two-tailed unpaired Student's t-test.

J. Correlations between *AXIN2*, *LEF1*, *CD44*, and *GAS6* mRNA expression were analyzed by Pearson's correlation test according to the TCGA-CHOL datasets.

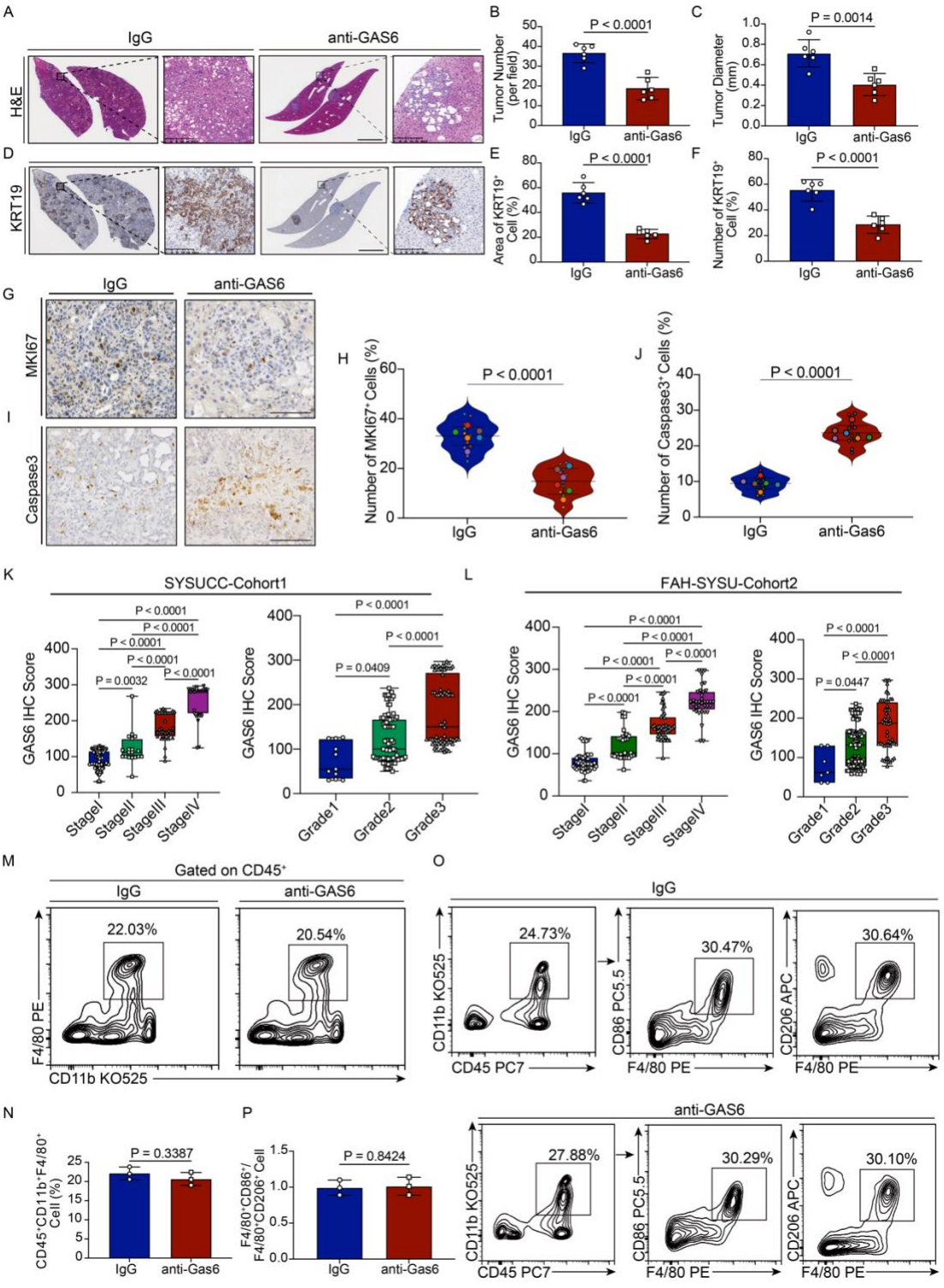

Figure S5 Related to Figure 4. Blocking of GAS6 led to inhibition of ICC development

A-F. Representative images of H&E staining (A) and KRT19 staining (D) of liver sections in ICC mice treated with anti-GAS6 or IgG, with scale bars of 200 μm. Statistical analyses include ICC number (B), ICC diameter (C), KRT19 area (E), and

KRT19$^+$ cells (F) in the anti-GAS6 and IgG groups. Values are mean ± SD from six independent biological replicates (n = 6 mice). *P* values were calculated by two-tailed unpaired Student's t-test.

G-J. Representative images of MKI67 (G) and active-Caspase3 (I) staining of liver sections and their respective statistical analyses of MKI67$^+$ cells (H) and active-Caspase3$^+$ cells (J) in the anti-GAS6 and IgG groups. Scale bars, 100 μm. Values are mean ± SD from six independent biological replicates (n = 12 fields from 6 mice). *P* values were calculated by two-tailed unpaired Student's t-test.

K. GAS6 IHC score in different tumor stages (left) and tumor grades (right) from SYSUCC cohort1. *P* values were calculated by one-way ANOVA with Tukey's multiple comparison test.

L. GAS6 IHC score in different tumor stages (left) and tumor grades (right) from FAH-SYSU cohort2. *P* values were calculated by one-way ANOVA with Tukey's multiple comparison test.

M-P. In a multi-color DC profiling panel, SSC and FSC parameters were used to isolate mononuclear cells, and CD45$^+$ mononuclear cells were confirmed as immune cells. Macrophages were defined as CD11b$^+$F4/80$^+$, M1 macrophages identified as F4/80$^+$CD86$^+$ and M2 macrophages as F4/80$^+$CD206$^+$. Representative flow plots show the frequency of these specific cell clusters in the anti-GAS6 and IgG groups (M, O). Quantification includes CD11b$^+$F4/80$^+$ cells (N) and the ratios of F4/80$^+$CD86$^+$/F4/80$^+$CD206$^+$ cells (P) in different groups. Values are mean ± SD from three independent experiments (n = 3 mice). *P* values were calculated by two-tailed unpaired Student's t-test.

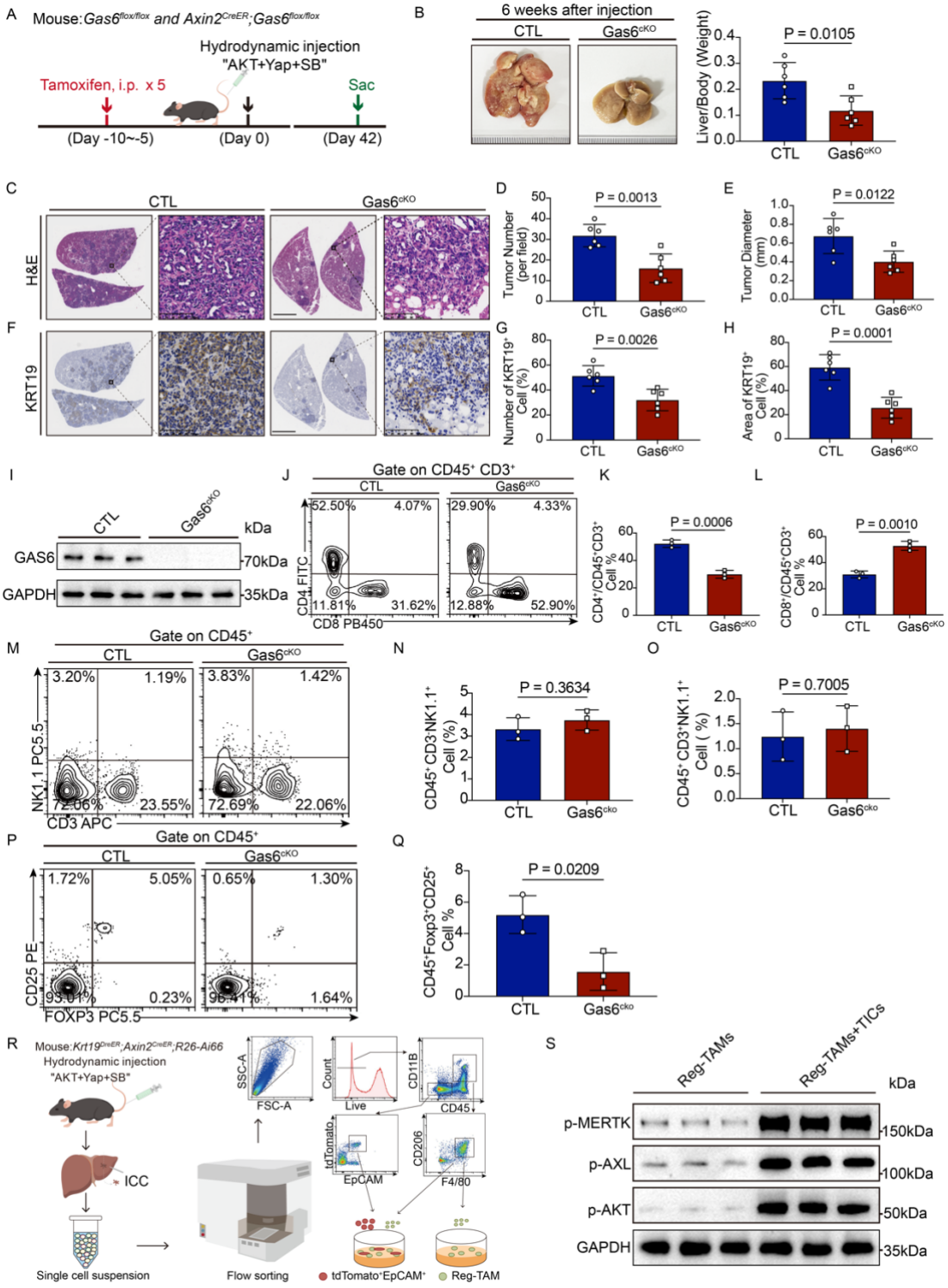

Figure S6. Related to Figure 4. Epithelial-specific knockout of GAS6 leads to the inhibition of ICC development

A. Experimental design for induction of ICC in *Gas6*$^{flox/flox}$ (Control group) and *Axin2-creER; Gas6*$^{flox/flox}$ (Gas6^{cko} group) mice. The mice were sacrificed six weeks after the plasmids were injected.

B. Representative image of whole liver morphology in control and Gas6^{cKO} mice with the plasmid injected for six weeks (left). Statistical analysis of liver to body weight ratio in control and Gas6^{cKO} mice (right). Values are mean ± SD from six independent biological replicates (n = 6 mice). *P* value was calculated by two-tailed unpaired Student's t-test.

C-H. Representative images of H&E staining (C) and KRT19 staining (F) of liver sections in control and Gas6^{cKO} groups, with scale bars of 100 μm. Statistical analysis of ICC number (D), ICC diameter (E), KRT19^{+} cells (G), and KRT19^{+} area (H) in control and Gas6^{cKO} groups. Values are mean ± SD from six independent biological replicates (n = 6 mice). *P* values were calculated by two-tailed unpaired Student's t-test.

I. The knockout efficiency of GAS6 in Axin2^{+} cells was validated by WB analysis.

J-L. Representative flow plots showing the frequency of CD4^{+} and CD8^{+} T cells in control and Gas6cKO mice (J). Statistical analysis of the number of CD4^{+} (K) and CD8^{+} (L) T cells in control and Gas6^{cKO} mice. Values are mean ± SD from three independent experiments (n = 3 mice). *P* values were calculated by two-tailed unpaired Student's t-test.

M-O. Representative flow plots showing the frequency of NK and NKT cells in control and Gas6^{cKO} mice (M). Statistical analysis of the number of NK cells (N) and NKT cells (O) in control and Gas6^{cKO} mice. Values are mean ± SD from three independent experiments (n = 3 mice). *P* values were calculated by two-tailed unpaired Student's t-test.

P-Q. Representative flow plots showing the frequency of CD25^{+} Foxp3^{+} cells in control and Gas6^{cKO} mice (P). Statistical analysis of the number of CD25^{+} Foxp3^{+} cells in control and Gas6^{cKO} mice (Q). Values are mean ± SD from three independent experiments (n = 3 mice). *P* value was calculated by two-tailed unpaired Student's t-test.

R. The schematic diagram illustrating the sorting and co-culture of TICs and Reg-TAM cells.

S. Western blot analysis of phosphorylated AXL, MERTK, AKT, and GAPDH in ICC Reg-TAMs co-cultured with or without TICs treatments.

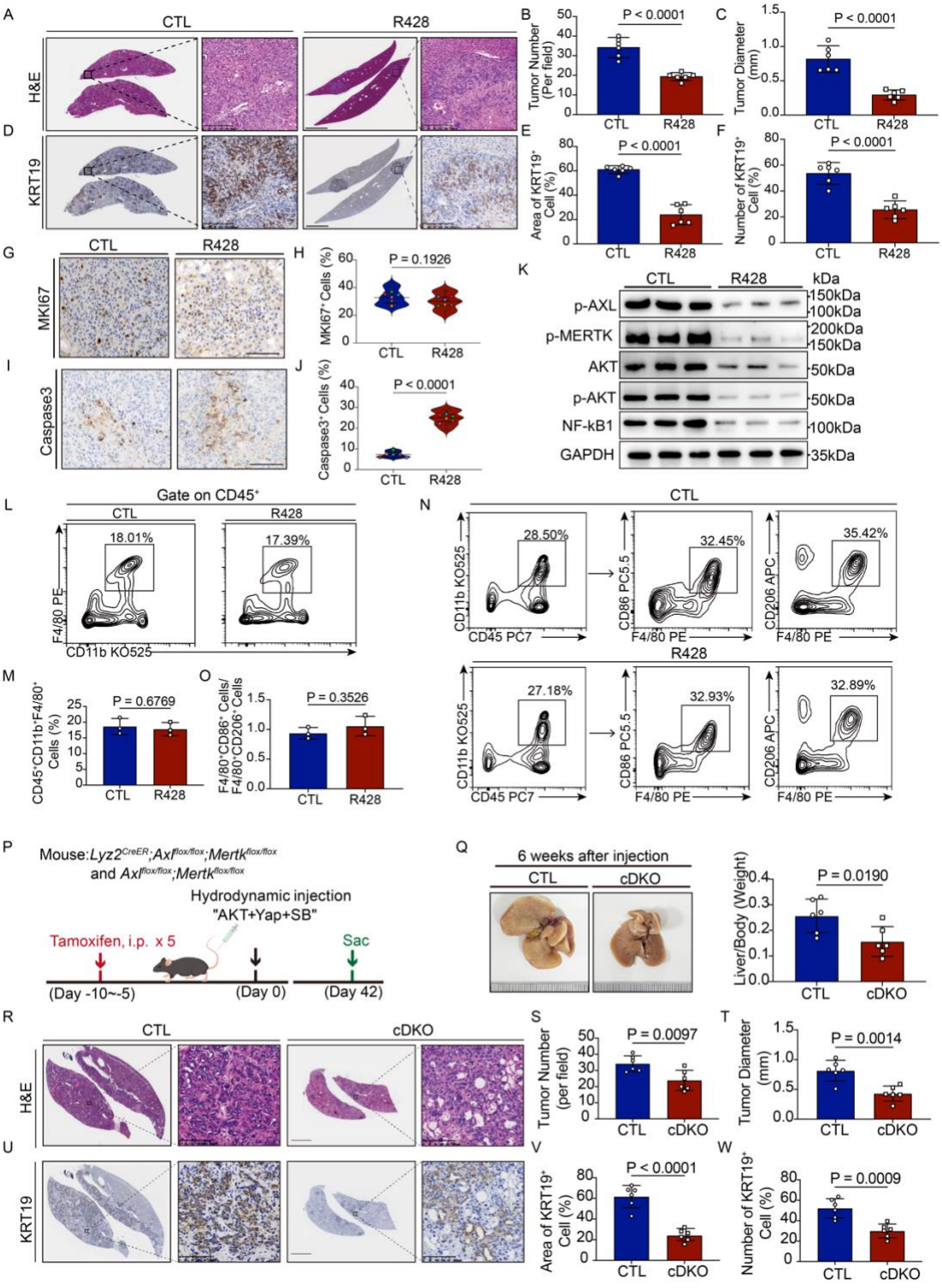

Figure S7 Related to Figure 5. Treatment with R428 or double knockout of *Axl* and *Mertk* inhibited ICC formation

A-F. Representative images of H&E staining (A) and KRT19 staining (D) of liver sections in ICC mice from R428 treatment or control groups. Scale bar, 200 μm.

Statistical analysis of ICC number (B), ICC diameter (C), KRT19 area (E), and KRT19$^+$ cells (F) in different groups. Values are mean ± SD from six independent biological replicates (n = 6 mice). *P* values were calculated by two-tailed unpaired Student's t-test.

G-J. Representative images of MKI67 (G) and active-Caspase3 (I) staining of liver sections in the R428 treatment or control groups. Scale bar, 100 μm. Statistical analysis of MKI67$^+$ (H) and active-Caspase3$^+$ (J) cells in the same groups. Values are mean ± SD from six independent biological replicates (n = 12 fields from 6 mice). *P* values were calculated by two-tailed unpaired Student's t-test.

K. Western blot analysis of p-AXL, p-MERTK, p-AKT, AKT, NF-κB1, and GAPDH in Reg-TAMs with or without R428 treatment, after co-culturing with EpCAM$^+$ Tom$^+$ TICs.

L and M. Representative flow plots show the frequency of the CD11b$^+$ F4/80$^+$ macrophages as indicated in the control and R428 group (L). Quantification of the CD11b$^+$ F4/80$^+$ cells in control and R428 group (M). Values are mean ± SD (n = 3 mice). *P* value was calculated by two-tailed unpaired Student's t-test.

N and O. Representative flow plots show the frequency of the F4/80$^+$CD86$^+$ macrophages and F4/80$^+$CD206$^+$ macrophages as indicated in the control and R428 group (N). Quantification of the ratios of F4/80$^+$CD86$^+$/ F4/80$^+$CD206$^+$ cells in WT and R428 group (O). *P* value was calculated by two-tailed unpaired Student's t-test.

P. Experimental design for induction of ICC in *Axl*$^{flox/flox}$; *Mertk*$^{flox/flox}$ (Control group, CTL) and *Lyz2-CreER; Axl*$^{flox/flox}$; *Mertk*$^{flox/flox}$ (*Axl* and *Mertk* conditional double knockout, cDKO group) mice. The mice were sacrificed six weeks after the plasmids were injected.

Q. Representative image of whole liver morphology in CTL and cDKO mice with the plasmid injected for six weeks (left). Statistical analysis of liver to body weight ratio in CTL and cDKO mice (right). Values are mean ± SD from six independent biological replicates (n = 6 mice). *P* value was calculated by two-tailed unpaired Student's t-test.

R-W. Representative images of H&E (R) and KRT19 (U) staining of liver sections in different treatment groups, with scale bars of 100 μm. Statistical analysis of ICC number (S), ICC diameter (T), KRT19$^+$ area (V), and KRT19$^+$ cells (W) in CTL and

cDKO groups. Values are mean ± SD from six independent biological replicates (n = 6 mice). *P* values were calculated by two-tailed unpaired Student's t-test.

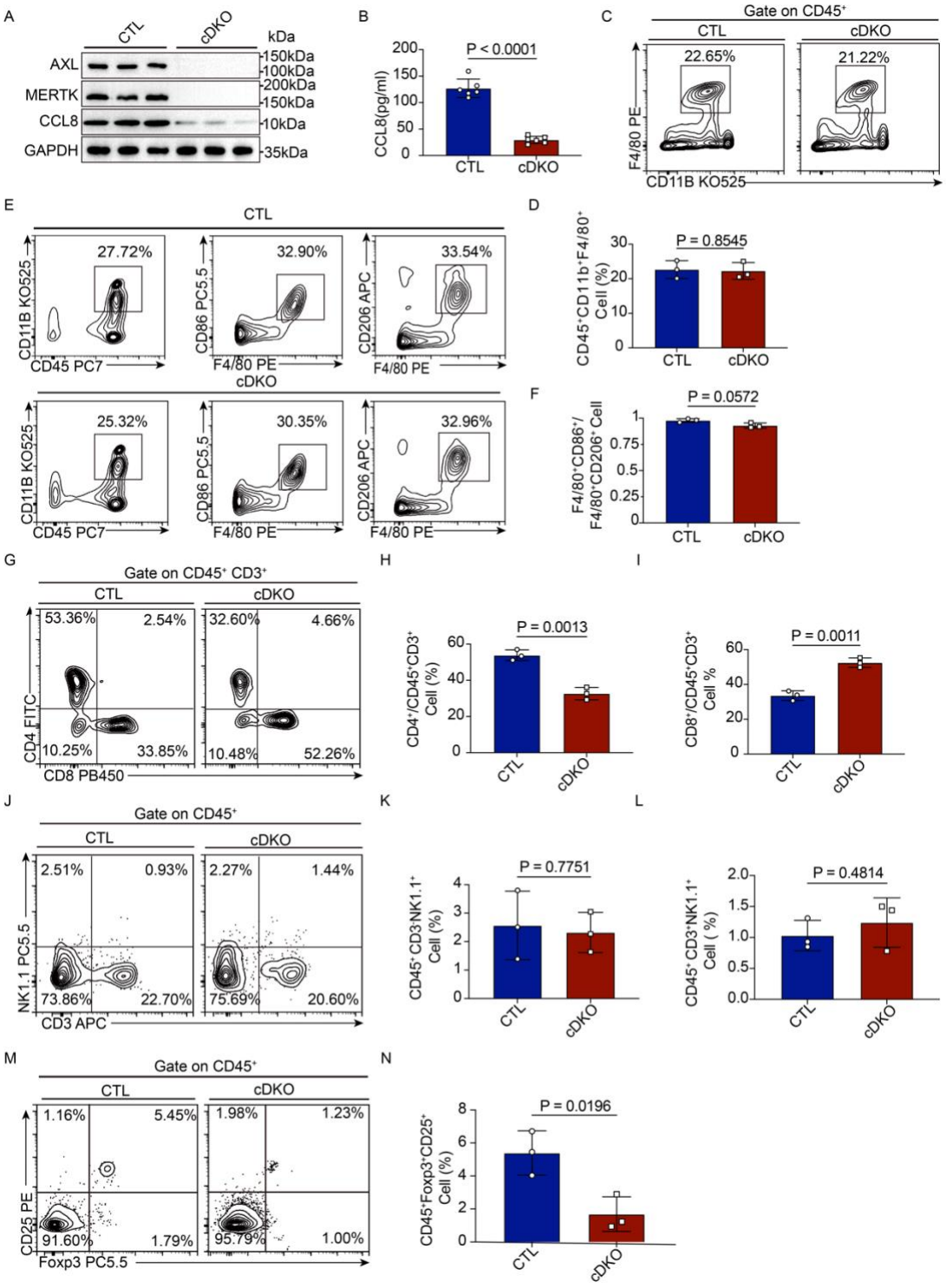

Figure S8 Related to Figure 5. Conditional knockout of *Axl* and *Mertk* inhibited ICC formation.

A. Western blotting analysis of AXL, MERTK, CCL8, and GAPDH in ICC Reg-TAMs in Control (CTL group) and *Lyz2-CreER; Axl*$^{flox/flox}$*; Mertk*$^{flox/flox}$ (*Axl* and *Mertk* conditional double knockout, cDKO group) mice.

B. ELISA showed the protein levels of CCL8 in Reg-TAMs between CTL and cDKO groups. Values are mean ± SD from six independent biological replicates (n = 6 mice). *P* value was calculated by two-tailed unpaired Student's t-test.

C and D. Representative flow plots show the $CD11b^+F4/80^+$ macrophage frequency as indicated in CTL and cDKO groups (C). Quantification of the $CD11b^+F4/80^+$ cells in CTL and cDKO groups (D). Values are mean ± SD (n = 3 mice). *P* value was calculated by two-tailed unpaired Student's t-test.

E and F. Representative flow plots show the frequency of the $F4/80^+CD86^+$ macrophages and $F4/80^+CD206^+$ macrophages as indicated in CTL and cDKO groups (E). Quantification of the ratios of $F4/80^+CD86^+$/ $F4/80^+CD206^+$ cells in CTL and cDKO groups (F). *P* value was calculated by two-tailed unpaired Student's t-test.

G-I. Representative flow plot showing the frequency of $CD4^+$ and $CD8^+$ T cells in CTL and cDKO mice (G). Statistical analysis of the number of $CD4^+$ (H) and $CD8^+$ (I) T cells in CTL and cDKO mice. Values are mean ± SD from three independent experiments (n = 3 mice). *P* values were calculated by two-tailed unpaired Student's t-test.

J-L. Representative flow plot showing the frequency of NK and NKT cells in CTL and cDKO mice (J). Statistical analysis of the number of NK (K) and NKT (L) cells in CTL and cDKO mice. Values are mean ± SD from three independent experiments (n = 3 mice). *P* values were calculated by two-tailed unpaired Student's t-test.

M and N. Representative flow plot showing the frequency of $CD25^+$ $Foxp3^+$ cells in CTL and cDKO mice. Statistical analysis of the number of $CD25^+$ $Foxp3^+$ cells in CTL and cDKO mice. Values are mean ± SD from three independent experiments (n = 3 mice). *P* value was calculated by two-tailed unpaired Student's t test.

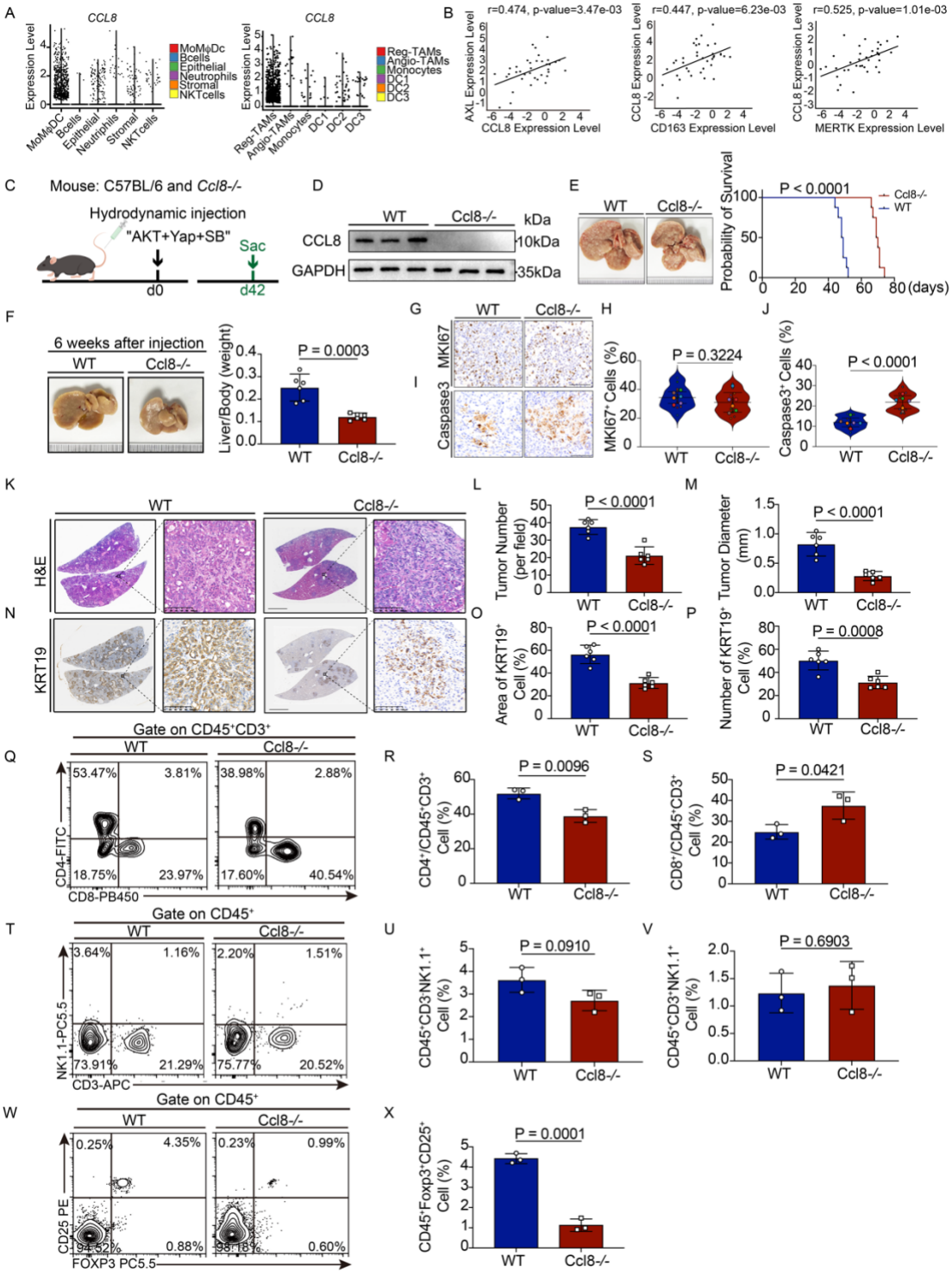

Figure S9 Related to Figure 6. CCL8 is the downstream mediator of AXL signaling in Reg-TAMs

A. Violin plots showed expression of *AXL* in all six clusters (left) and MoMϕDC clusters (right) from human ICC tumor tissues.

B. Correlation between *AXL*, *CD163*, *MERTK*, and *CCL8* expression were analyzed by

Pearson's correlation test according to the TCGA-CHOL datasets.

C. Experimental design for induction of ICC in C57BL/6 (WT group) and *Ccl8-/-* (*Ccl8-/-* group) mice.

D. The knockout efficiency of *Ccl8* was validated by WB analysis.

E. Representative image of whole liver morphology in WT and *Ccl8-/-* KO mice (left). The time of mice developed lethal tumor burden was shown. The Kaplan-Meier overall survival curve of WT and *Ccl8-/-* mice (right). *P* value was calculated by log-rank test.

F. Representative image of whole liver morphology in WT and *Ccl8-/-* mice with the plasmid injected for six weeks (left). Statistical analysis of liver to body weight ratio in WT and *Ccl8-/-* mice (right). Values are mean ± SD from six independent biological replicates (n = 6 mice). *P* value was calculated by two-tailed unpaired Student's t-test.

G-J. Representative images of MKI67 (G) and active-Caspase3 (I) staining of liver sections from ICC mice in WT and *Ccl8-/-* groups, with scale bars of 100 μm. Statistical analysis of $MKI67^+$ (H) and active-$Caspase3^+$ cells (J) in WT and *Ccl8-/-* groups. Values are mean ± SD from six independent biological replicates (n = 12 fields from 6 mice). *P* values were calculated by two-tailed unpaired Student's t-test.

K-P. Representative images of H&E staining (K) and KRT19 staining (N) of liver sections from ICC mice in WT and *Ccl8-/-* groups, with scale bars of 100 μm. Statistical analyses include ICC number (L), ICC diameter (M), KRT19 area (O), and $KRT19^+$ cells (P) in WT and *Ccl8-/-*groups. Values represent mean ± SD from six independent biological replicates (n = 6 mice). *P* values were calculated by two-tailed unpaired Student's t-test.

Q-S. Representative flow plots showing the frequency of $CD4^+$ and $CD8^+$ T cells in WT and *Ccl8-/-* mice (Q, left). Statistical analysis of the number of $CD4^+$ (R) and $CD8^+$ (S) T cells in WT and *Ccl8-/-* mice (right). Values represent mean ± SD from three independent experiments (n = 3 mice). *P* values were calculated by two-tailed unpaired Student's t-test.

T-V. Representative flow plots showing the frequency of NK and NKT cells in WT and *Ccl8-/-* mice (T). Statistical analysis of the number of NK (U) and NKT (V) cells in WT and *Ccl8-/-* mice. Values are mean ± SD from three independent experiments (n =

3 mice). *P* values were calculated by two-tailed unpaired Student's t-test.

W-X. Representative flow plots showing the frequency of $CD25^+$ $Foxp3^+$ cells in WT and *Ccl8-/-* mice (W). Statistical analysis of the number of $CD25^+$ $Foxp3^+$ cells in WT and *Ccl8-/-* mice (X). Values are mean ± SD from three independent experiments (n = 3 mice). *P* values were calculated by two-tailed unpaired Student's t-test.

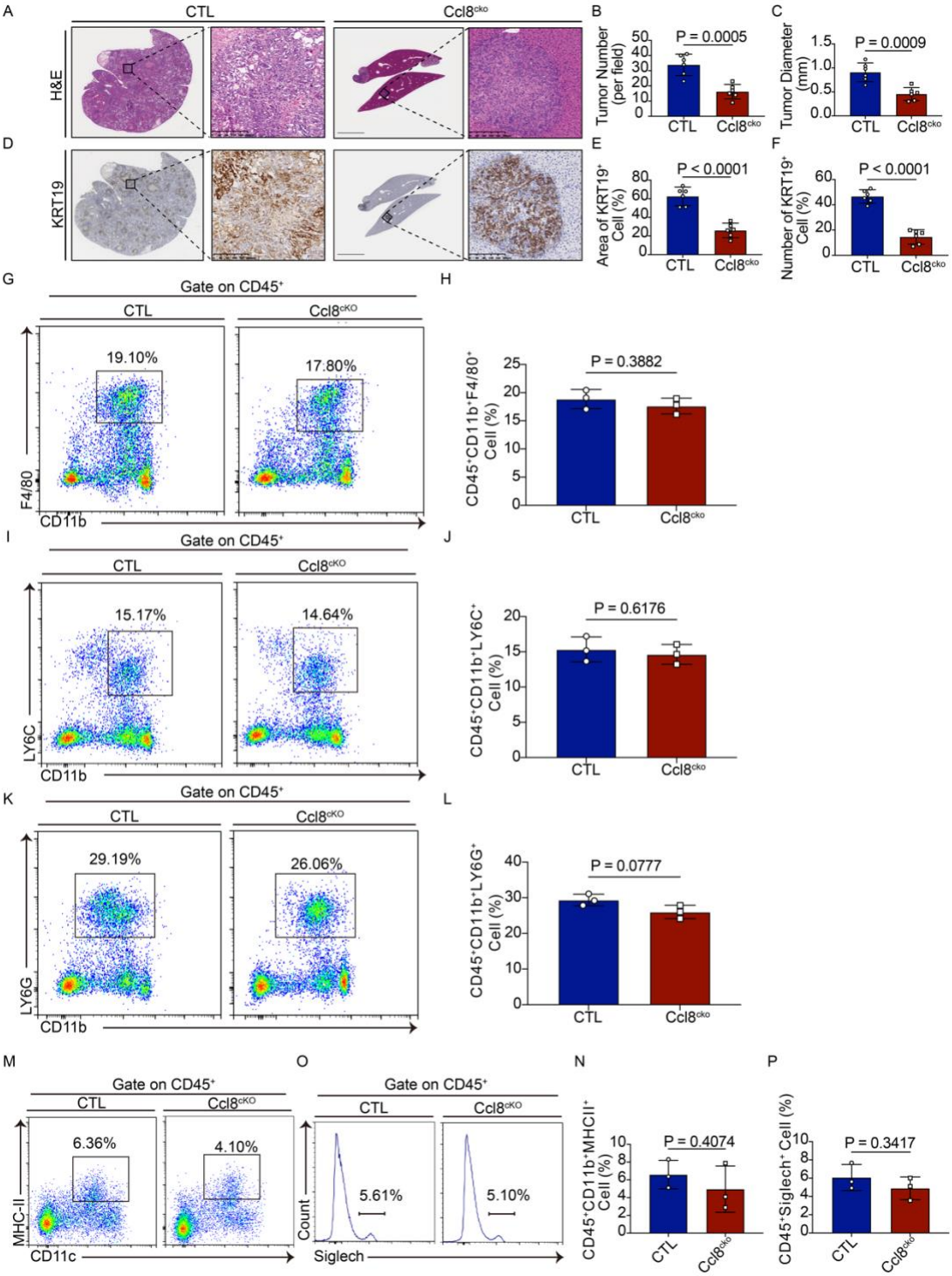

Figure S10 Related to Figure. CCL8 is the downstream mediator of AXL signaling in Reg-TAMs.

A-F. Representative images of H&E staining (A) and KRT19 staining (D) of liver sections in control (CTL) and *Lyz2-creER; Ccl8$^{flox/flox}$* (Ccl8^{cKO}) groups, with scale bars of 200 μm. Statistical analyses include ICC number (B), ICC diameter (C), KRT19^{+}

cells (E), and KRT19^{+} area (F) in CTL and Ccl8^{cKO} groups. Values represent mean ± SD from six independent biological replicates (n = 6 mice). *P* values were calculated by two-tailed unpaired Student's t-test.

G and H. Representative flow plots show the frequency of the CD11b^{+} F4/80^{+} macrophages as indicated in CTL and Ccl8^{cKO} groups (G). Quantification of the CD11b^{+} F4/80^{+} cells in CTL and Ccl8^{cKO} groups (H). Values are mean ± SD (n = 3 mice). *P* value was calculated by two-tailed unpaired Student's t-test.

I and J. Representative flow plots show the frequency of the CD11b^{+} LY6C^{+} monocytes as indicated in CTL and Ccl8^{cKO} groups (I). Quantification of the CD11b^{+} LY6C^{+} cells in CTL and Ccl8^{cKO} groups (J). Values are mean ± SD (n = 3 mice). *P* value was calculated by two-tailed unpaired Student's t-test.

K and L. Representative flow plots show the frequency of the CD11b^{+} LY6G^{+} neutrophils as indicated in CTL and Ccl8^{cKO} groups (K). Quantification of the CD11b^{+} LY6G^{+} cells in CTL and Ccl8^{cKO} groups (L). Values are mean ± SD (n = 3 mice). *P* value was calculated by two-tailed unpaired Student's t-test.

M and N. Representative flow plots show the frequency of the CD11c^{+} MHC II^{+} cDCs as indicated in CTL and Ccl8^{cKO} groups (M). Quantification of the CD11c^{+} MHC II^{+} cells in CTL and Ccl8^{cKO} groups (N). Values are mean ± SD (n = 3 mice). *P* value was calculated by two-tailed unpaired Student's t-test.

O and P. Representative histogram plots show the frequency of the Siglech^{+} pDCs as indicated in CTL and Ccl8^{cKO} groups (O). Quantification of the Siglech^{+} cells in CTL and Ccl8^{cKO} groups (P). Values are mean ± SD (n = 3 mice). *P* value was calculated by two-tailed unpaired Student's t-test.

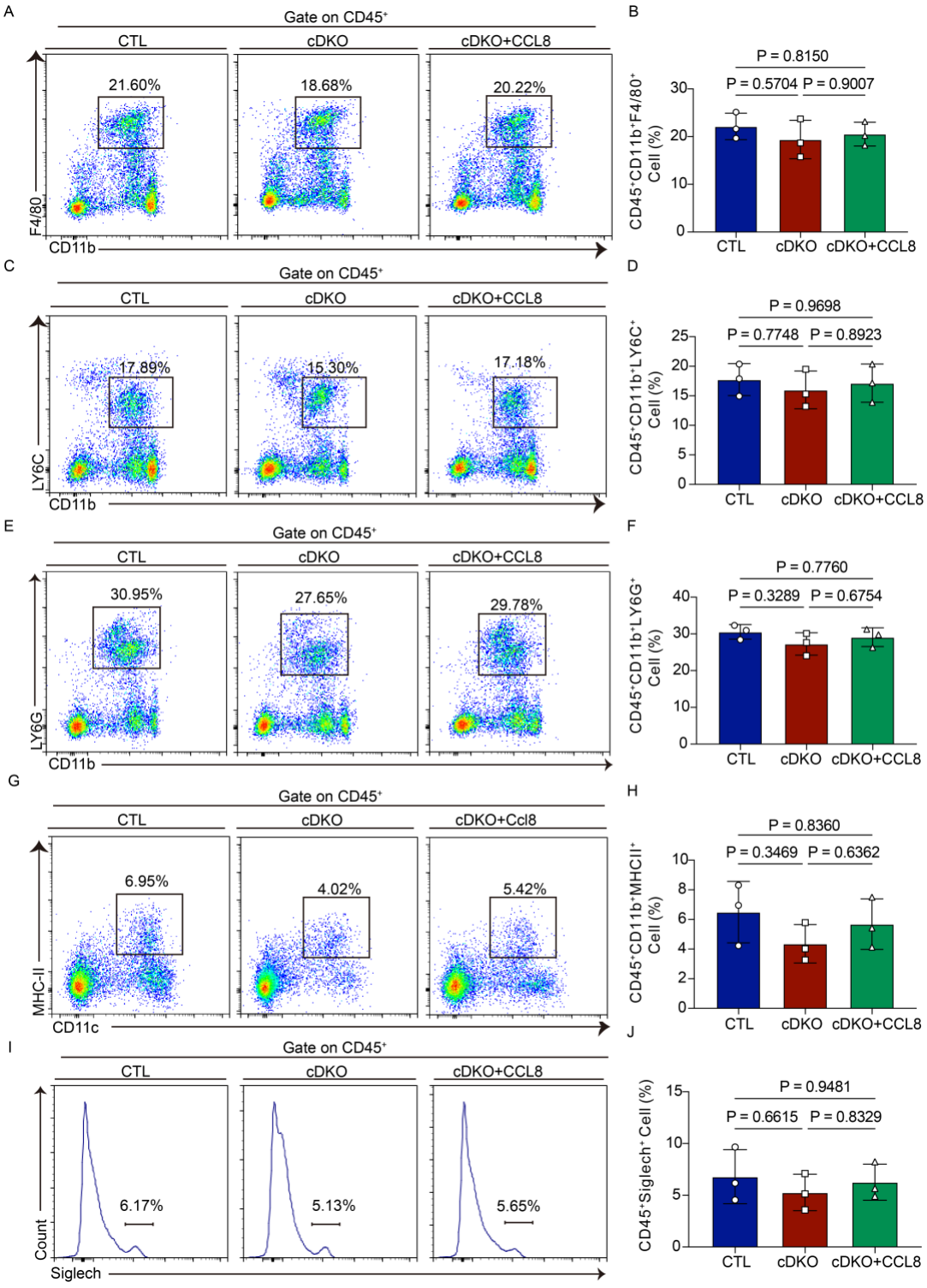

Figure S11 Related to Figure. CCL8 is the downstream mediator of AXL signaling in Reg-TAMs

A and B. Representative flow plots show the frequency of the CD11b^{+} F4/80^{+} macrophages as indicated in control (CTL), *Lyz2-creER; Axl$^{flox/flox}$; Mertk$^{flox/flox}$* (Double

Knockout, cDKO group) and *Lyz2-creER; Axl$^{flox/flox}$; Mertk$^{flox/flox}$* +CCL8 (cDKO+CCL8) groups (A). Quantification of the CD11b^{+} F4/80^{+} cells in CTL, cDKO, and cDKO+CCL8 groups (B). Values are mean ± SD (n = 3 mice). *P* values were calculated by one-way ANOVA with Tukey's multiple comparison test.

C and D. Representative flow plots show the frequency of the CD11b^{+} LY6C^{+} monocytes as indicated in CTL, cDKO, and cDKO+CCL8 groups (C). Quantification of the CD11b^{+} LY6C^{+} cells in CTL, cDKO, and cDKO+CCL8 groups (D). Values are mean ± SD (n = 3 mice). *P* values were calculated by one-way ANOVA with Tukey's multiple comparison test.

E and F. Representative flow plots show the frequency of the CD11b^{+} LY6G^{+} neutrophils as indicated in CTL, cDKO, and cDKO+CCL8 groups (E). Quantification of the CD11b^{+} LY6G^{+} cells in CTL, cDKO, and cDKO+CCL8 groups (F). Values are mean ± SD (n = 3 mice). *P* values were calculated by one-way ANOVA with Tukey's multiple comparison test.

G and H. Representative flow plots show the frequency of the CD11c^{+} MHC II^{+} cDCs as indicated in CTL, cDKO, and cDKO+CCL8 groups (G). Quantification of the CD11c^{+} MHC II^{+} cells in CTL, cDKO, and cDKO+CCL8 groups (H). Values are mean ± SD (n = 3 mice). *P* values were calculated by one-way ANOVA with Tukey's multiple comparison test.

I and J. Representative histogram plots show the frequency of the Siglech^{+} pDCs as indicated in CTL, cDKO, and cDKO+CCL8 groups (I). Quantification of the Siglech^{+} cells in CTL, cDKO, and cDKO+CCL8 groups (J). Values are mean ± SD (n = 3 mice). *P* values were calculated by one-way ANOVA with Tukey's multiple comparison test.

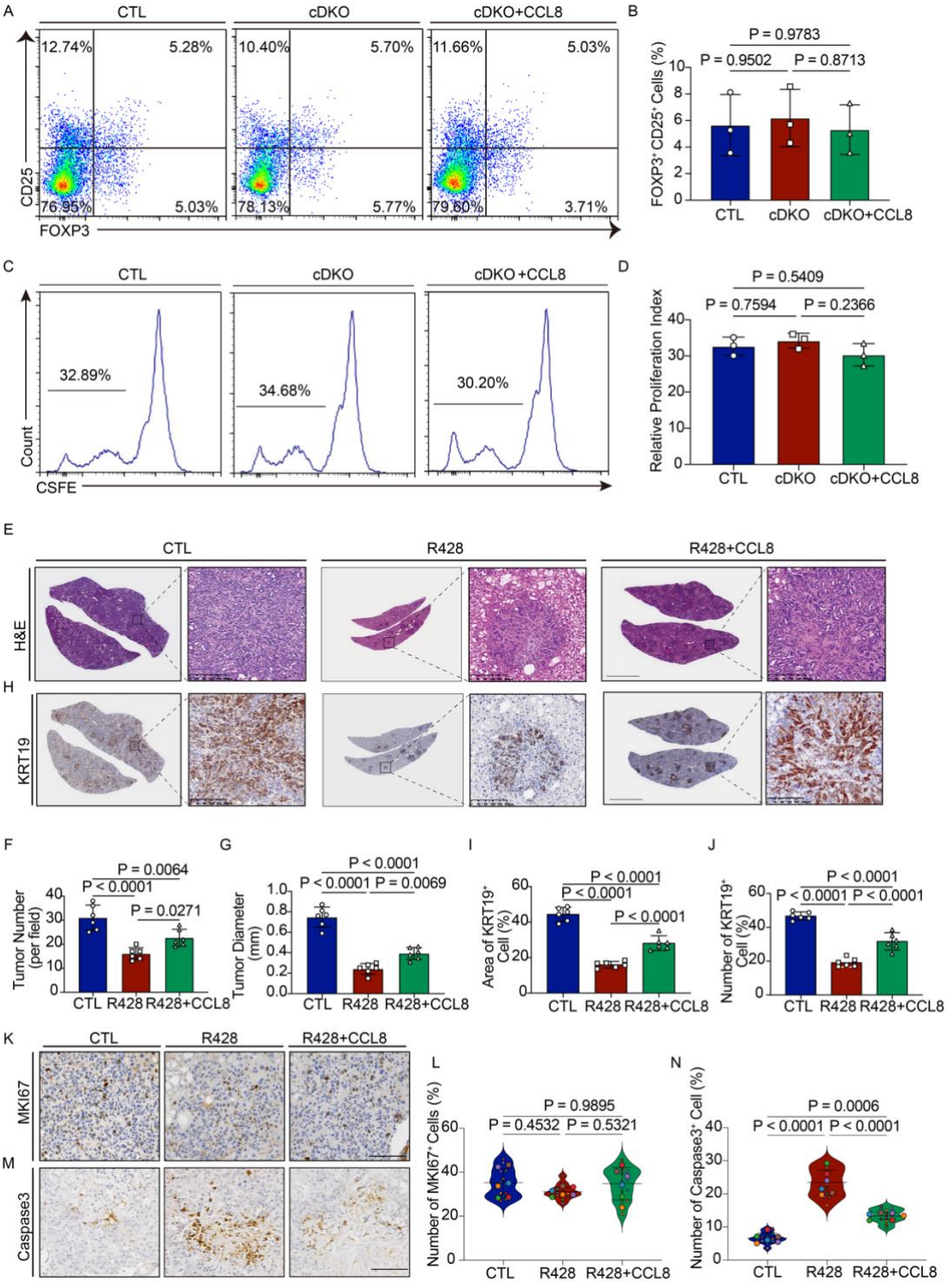

Figure S12 Related to Figure. CCL8 is the downstream mediator of AXL signaling in Reg-TAMs

A and B. Representative flow plots (A) and corresponding graph of the frequency of $CD25^{+}Foxp3^{+}$ Treg cells in control (CTL), *Lyz2-creER; Axl*$^{flox/flox}$*; Mertk*$^{flox/flox}$ (*Axl* and *Mertk* conditional double knockout, cDKO group) and *Lyz2-creER; Axl*$^{flox/flox}$*;*

Mertk$^{flox/flox}$ +CCL8 (cDKO+CCL8) groups(B). Values are mean ± SD from three independent experiments (n = 3 mice). *P* values were calculated by one-way ANOVA with Tukey's multiple comparison test.

C and D. Representative histograms show CFSE intensity of $CD3^+CD8^+$ T cells (C) and the corresponding relative proliferation index (D) in CTL, cDKO, and cDKO+CCL8 groups, as assessed by flow cytometry. Values are mean ± SD from three independent experiments (n = 3 mice), and *P* values were calculated by one-way ANOVA with Tukey's multiple comparison test.

E-J. Representative images of H&E staining (E) and KRT19 staining (H) of liver sections in different treatment groups, with scale bars of 200 μm. Statistical analyses include ICC number (F), ICC diameter (G), $KRT19^+$ cells (I), and $KRT19^+$ area (J) across different treatment groups. Values represent mean ± SD from six independent biological replicates (n = 6 mice). *P* values were calculated by one-way ANOVA with Tukey's multiple comparison test.

K and M. Representative images of MKI67 (K) and active-Caspase3 (M) staining of liver sections in different treatment groups. Scale bar, 100μm.

L and N. Statistical analysis of $MKI67^+$ (L) and active-$Caspase3^+$ cells (N) in different treatment groups. Values are mean ± SD from six independent biological replicates (n = 12 fields from 6 mice). *P* values were calculated by one-way ANOVA with Tukey's multiple comparison test.

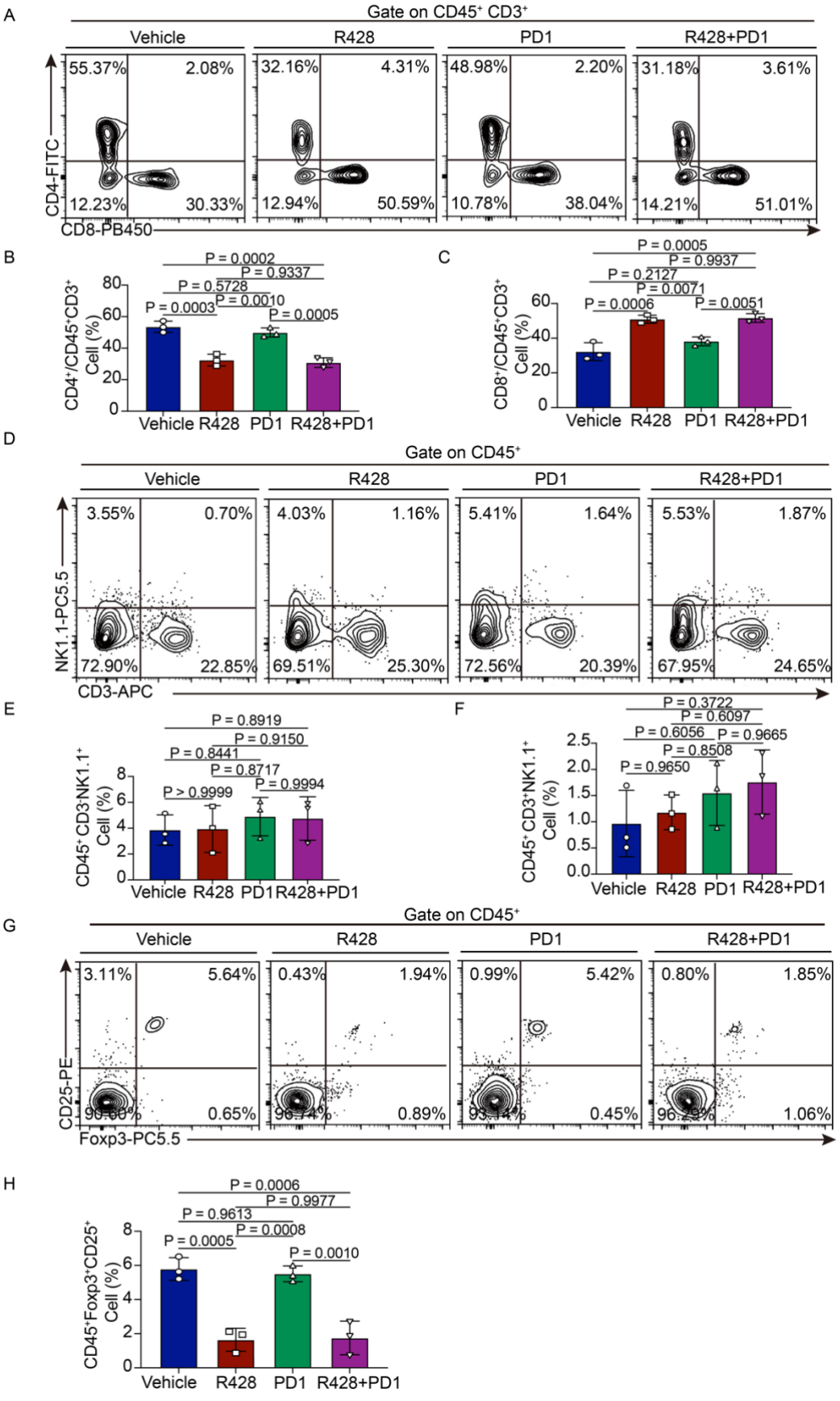

Figure S13. Related to Figure 7. R428 treatment sensitizes murine ICC cells to anti-

PD-1 treatment

A-C. Representative flow plots (A) and corresponding graphs of the frequency of tumor-infiltrating $CD4^+$ (B), and $CD8^+$ (C) T cells in different treatment groups. Error bars are mean ± SD from three independent experiments (n = 3 mice). *P* values were calculated by one-way ANOVA with Tukey's multiple comparison test.

D-F. Representative flow plots (D) and corresponding graphs of the frequency of tumor-infiltrating NK cells (E) and tumor-infiltrating NKT cells (F) in different treatment groups. Error bars are mean ± SD from three independent experiments (n = 3 mice). *P* values were calculated by one-way ANOVA with Tukey's multiple comparison test.

G and H. Representative flow plots (G) and corresponding graph of the frequency of tumor-infiltrating Treg cells (H) in different treatment groups. Values are mean ± SD from three independent experiments (n = 3 mice). *P* values were calculated by one-way ANOVA with Tukey's multiple comparison test.

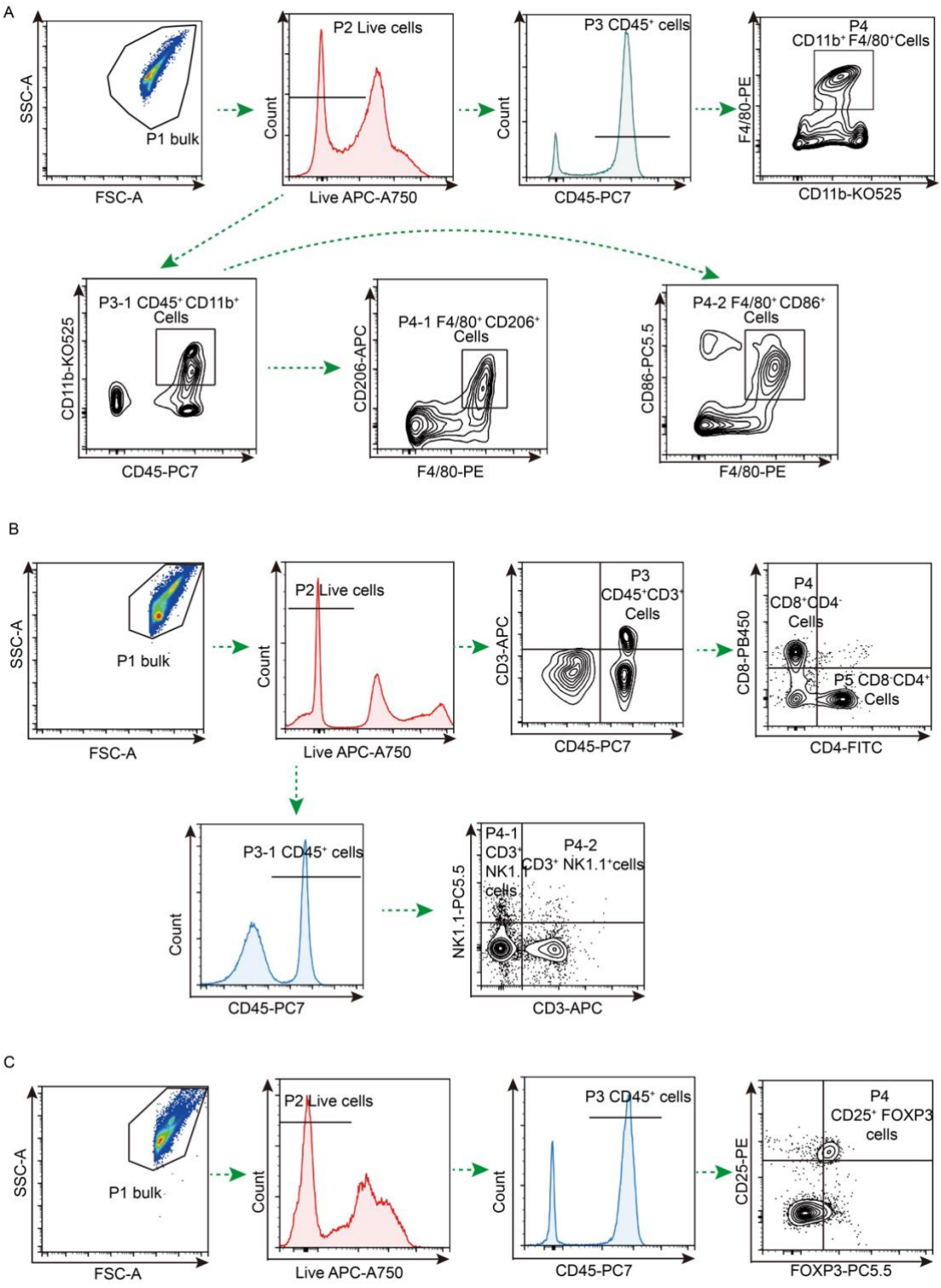

Figure S14. Flow cytometry gating strategies

A-C. Gating strategies were used in this study to define different macrophage populations (A), T cell populations (B), and Tregs (C).